12-2022

Investigation of Process Parameters to Fabricate Refractory Medium-Entropy Alloy by Selective Laser Melting Process

Abdullah Al Masum Jabir
The University of Texas Rio Grande Valley

INVESTIGATION OF PROCESS PARAMETERS TO FABRICATE REFRACTORY

MEDIUM-ENTROPY ALLOY BY SELECTIVE LASER MELTING PROCESS.

A Thesis

by

ABDULLAH AL MASUM JABIR

Submitted in Partial Fulfillment of the

Requirements for the Degree of

MASTER OF SCIENCE IN ENGINEERING

Major Subject: Manufacturing Engineering

The University of Texas Rio Grande Valley

December 2022

INVESTIGATION OF PROCESS PARAMETERS TO FABRICATE REFRACTORY

MEDIUM-ENTROPY ALLOY BY SELECTIVE LASER MELTING PROCESS.

A Thesis
by
ABDULLAH AL MASUM JABIR

COMMITTEE MEMBERS

Dr. Jianzhi Li
Chair of Committee

Dr Farid Ahmed
Committee Member

Dr Zhaohio Geng
Committee Member

Dr Rajiv Nambiar
Committee Member

December 2022

ABSTRACT

Jabir, Abdullah Al Masum, <u>Investigation on Process parameters to Fabricate Refractory Medium-Entropy Alloy by Selective Laser Melting Process.</u> Master of Science in Engineering (MSE), December 2022, 66 pp, 10 tables, 23 figures, references, 120 titles.

This thesis proposal investigates the synthesis of TiWMo refractory medium entropy alloy (RMEA) by selective laser melting process from elemental powder. Steel, titanium and tungsten substrates were used to study the impact on the formation of TiWMo RMEA. Different process parameters were applied to investigate the effects on melting, diffusion and formation of RMEA. The microstructure of TiWMo and elemental distribution were observed by scanning electron microscope (SEM) and energy dispersive X-ray spectroscopy (EDS). SEM analysis revealed that with higher energy density the pores and microcracks were improved. EDS data validated the composition is homogenized and stable after few layers of deposition. Single phase BCC solid solution was predicted based on the theoretical calculation. The maximum microhardness 644 HV achieved from the highest 350 J/mm^3 energy density.

DEDICATION

My thesis wouldn't be completed without tremendous support from my mother, Jahanara Akther, my father, Md. Moazzem Hossain, my lovely wife, Zannat Ara, my elder sisters, Mishkat Jahan Nishu, Farjana Jahan Shimu and my elder brother Abdullah Al Mamun Shohag. Those people always inspired me to move forward. Gave me strength to survive. Additionally, my supervisor Dr James Li and mentor Dr Lee also supported me a lot.

ACKNOWLEDGMENTS

TABLE OF CONTENTS

LIST OF TABLES

LIST OF FIGURES

CHAPTER I

INTRODUCTION

The majority of conventional alloys are made up of just one main constituent. To increase the properties, different minor elements are added to the main constituent and form different alloys. However, different types of binary alloys are restricted to the number of elements in the periodic table. To find a solution, a new idea of high entropy alloys (HEA) and multi-principal element alloys (MPEA) came. The first study was initiated on multi-principle element alloys in late 1970 and was later expanded the work in 1998 and then published in 2004 (Cantor, Chang, Knight, & Vincent, 2004) . In the same year, a new concept of HEA had been proposed by (J. W. Yeh et al., 2004). HEAs possess unique properties (for example, strength and toughness at extreme conditions (Ding et al., 2019; Yiping Lu et al., 2014; Tsai & Yeh, 2014)), wear resistance (Chuang, Tsai, Wang, Lin, & Yeh, 2011) and fatigue (Hemphill et al., 2012) due to their multi-element composition. Those unique features make HEA appealing in a variety of sectors.

Many of these HEAs, which formed from cobalt, chromium, nickel, titanium, vanadium, manganese, iron and copper have good mechanical properties and can reach yield strengths of more than 1000 MPa at temperatures below 600°C (O. N. Senkov, Miracle, Chaput, & Couzinie, 2018). Unfortunately, none of the reported HEAs exhibit high yield strengths at high temperature that are superior to sophisticated Ni-based superalloys (Gorsse, Miracle, & Senkov, 2017) . The high-temperature strength of HEAs, like that of Ni-based superalloys, rapidly declines beyond 800

°C. Therefore, at extreme temperatures, the Ni-based superalloys or alloys hold melting temperatures close to 1100^0C restricting their application at high temperatures. This limitation promoted to work with high melting temperature elements, which retain their strength at high temperature (O. N. Senkov et al., 2011).

Refractory high entropy alloys (RHEAs) were first made available in 2010 (O. Senkov, Wilks, Miracle, Chuang, & Liaw, 2010) and quickly became popular because they could keep their strength up to 1600 °C. There were only five refractory elements in the first two RHEAs ($V_{20}Nb_{20}Mo_{20}Ta_{20}W_{20}$ and $Nb_{25}Mo_{25}Ta_{25}W_{25}$). The next refractory alloys were developed based on nine elements from groups IV (titanium, zirconium and hafnium) , V (vanadium, namibium and tantalum), and VI (chromium, molybdenum and tungsten).

A new way to make RHEAs is to use powder metallurgy (PM) in combination with milling and/or mechanical alloying (Dobbelstein, Thiele, Gurevich, George, & Ostendorf, 2016; Kang, Lee, Ryu, & Hong, 2018; B. Liu, Wang, Chen, Fang, & Liu, 2017; Waseem, Lee, Lee, & Ryu, 2018). To produce the appropriate composition, elemental or pre-alloyed powders are mixed, and a compact product is generated using consolidation processes such as spark plasma sintering (SPS) under a vacuum. (B. Liu et al., 2017; Waseem et al., 2018). Powder Metallurgy (PM)-produced RHEAs have a finer grain structure and a more uniform content. During preparation, however, extra caution is required to prevent contamination and internal oxidation(B. Liu et al., 2017). In alloys with large W concentrations, iron can easily contaminate from the container walls, and another contamination (most frequently O and N) from the surroundings is common, particularly if reactive metals like titanium and zirconium exist in the alloy (Suryanarayana, 2001). These pollutants are tough to prevent, and their effects on the characteristics of consolidated materials may be severe. Selective laser melting (SLM) is a powder bed fusion process where the part is

produced layer by layer. This additive manufacturing (AM) process can handle elemental or pre-alloyed powder (Moghaddam, Shaburova, Samodurova, Abdollahzadeh, & Trofimov, 2021).

1.1 Definition of Alloys Based on Entropy

Total mixing entropy is the summation of configurational entropy, vibrational entropy, magnetic dipole entropy and electronic randomness entropy. However, configurational entropy dominates the total mixing entropy (Fultz, 2010; Swalin & Arents, 1962).

As per the Boltzmann's equation, the configurational entropy of a system can be calculated as

$$\Delta S_{conf} = k \ln w \tag{1}$$

Here, Boltzmann's constant is k and the number of ways the available energy can be combined or divided among the system's particles is w. The configurational entropy for an equimolar alloy can be calculated as below

$$\Delta S_{conf} = - k \ln w = - R \left(\frac{1}{n}\ln\frac{1}{n} + \frac{1}{n}\ln\frac{1}{n} + \cdots + \frac{1}{n}\ln\frac{1}{n} \right) = - R \ln\frac{1}{n} = R \ln n \tag{2}$$

As the number of elements grows, so does the entropy. During melting, per mole mixing entropy, ΔS_f, from solid to liquid is approximately one gas constant R. In a random solid solution, the mixing entropy per mole is higher, which reduces the free energy. According to Gibbs law, this lower free energy causes the stronger stability of solid solution phases. Therefore, configurational entropy has an impact on phase stability.

Below table 1 is showing the configurational entropies increasing with the increase of elements. We see the ternary alloy is 10% higher than R and the quinary alloy is 61% higher than R. Yeh et al. (J.-W. Yeh, 2013) put 1.5R as a boundary for high entropy and medium entropy alloy and 1R between medium and low entropy alloy. Because any alloy having

Table 1:Configurational entropies increase with the increase of elements (J.-W. Yeh, 2013).

N	ΔS_{conf}
1	0
2	0.69R
3	1.1R
4	1.39R
5	1.61R
6	1.79R
7	1.95R
8	2.08R
9	2.2R
10	2.3R
11	2.4R
12	2.49R
13	2.57R

mixing entropy below 1R could not overcome the atomic bonding energy. Below is the figure 1 showing the picture.

Figure 1: Alloy classification based on configurational entropy [12]

1.2 Problem Statement

The manufacturability of refractory multi-component alloy is complicated by high melting temperatures (1800 °C) and wide melting points of refractory materials (ranging from 1857 °C for Cr and Zr to 3422 °C for W). A different way to make RHEAs or RMEAs is using (PM) in combination with milling and/or mechanical alloying (Dobbelstein et al., 2016; Kang et al., 2018; B. Liu et al., 2017; Waseem et al., 2018). To produce the appropriate composition, elemental or pre-alloyed powders are mixed, also a compact product is generated using consolidation processes such as spark plasma sintering (SPS) under a vacuum (Kang et al., 2018; Waseem et al., 2018). However, extra caution is required to avoid contamination and internal oxidation (Kang et al., 2018). These pollutants are difficult to eliminate and may have a major influence on the characteristics of composite materials. SLM is one of the additive manufacturing powder bed-based methods that fabricates a 3D component layer-by-layer utilizing a high-energy laser beam to selectively melt and consolidate tiny layers of metal powders. AM technique allows for the production of complicated three-dimensional near-net shaped components without the use of dies, which is impossible to do with traditional methods (Chen, Gu, Xiong, & Xia, 2017). Components may be created to the same functional specifications with fewer materials because of the geometric flexibility provided by SLM. Metal AM's geometrical flexibility also enables the creation of lattice structures for weight reduction and the design of components for enhanced fluid dynamics (Burns, 2014; Nickels, 2016). Based on author's knowledge, fabricated RMEA by selective laser melting process. Additionally, The reported feedstock for these SLM-manufactured RHEAs is mostly mechanically alloyed powders (Luo et al., 2019), which have drawbacks such as high cost, limited material design freedom, and so on. As a result, it would be worthwhile to investigate the feasibility of fabricating RMEA from elemental metal powders.

During the SLM process for multi-component production, the laser melts the powders together and in the final construct, all of the metal elements have the same elemental distribution as they had before (L. Guo et al., 2021; Kim, Baek, Yang, & Lee, 2021; Litwa, Hernandez-Nava, Guan, Goodall, & Wika, 2021). However, ensuring that all of the particles in the mixture are properly dispersed is one of the most challenging elements of the multi-component manufacturing process when elemental powders are used rather than pre-alloyed powders. Even if all of the powders are correctly mixed, obtaining adequate diffusion among the various metal components in order to generate a random solid solution (SS) phase would be a considerable difficulty. The molten components take longer to cool down in traditional multi-component production procedures such arc melting, casting, and so on, and as a result, excellent diffusion between the elements occurs. SLM, on the other hand, is a highly fast solidification process (10^8 K/s (D. Gu et al., 2012)) in which the molten pool does not acquire enough cooling time to assure that the components diffuse as predicted. As a result, using the SLM technique to make multi-component alloys like RMEA with the correct elemental ratio is something worth looking into.

SLM fabrication components have a number of limitations that are influenced by a number of associated processing factors. For example, it has been discovered that non-optimal process settings result in large porosity and poor surface quality, which significantly reduces the mechanical performance of SLM as-built products (Gong et al., 2015; Kasperovich & Hausmann, 2015; Vayssette, Saintier, Brugger, Elmay, & Pessard, 2018). The energy density dictates the defect formation. The geographic distribution of defects is heavily influenced by scan strategy, with the majority of flaws occurring at both ends of scan tracks and between two neighboring

tracks (B. Zhang, Li, & Bai, 2017). So, optimizing the process parameters and figuring out their impact on the microstructure and mechanical properties of RMEA is really important.

1.3 Research Objectives

The objective of this research is

1. To investigate the feasibility of the fabrication of refractory medium entropy alloy from the elemental powder by SLM..

2. To study the impact of laser power and scanning speed with a fixed hatch distance on the microstructure and the mechanical properties of the alloy.

The elemental powder of W, Mo and Ti mixed together to ensure uniform distribution. The fabrication of refractory medium entropy alloy carried out by the EOS M 290 machine. Scanning Electron Microscope (SEM) used to see the morphology and microstructure. How does the diffusion take place. In the end, microhardness tested to check the mechanical properties.

1.4 Experimental Design and Methods

The experimental design and methods are the steps to follow in order to achieve the research objectives. Step 1, to mix the powder manually from elemental powders. . Step 2, to get the homogenous mixture, the powder will be mixed through a V-type blender. Step 3, the flowability test is done to check the powder flowability. Step 4, the EOS M 290 machine is used to fabricate the sample. Initially there were three processing parameters considered (laser power, scanning speed and hatch distance). For each factor, there were two levels (minimum value and maximum value) considered. So in total, there are 8 combinations of the parameters are considered.

Therefore, there will be 8 small cubes (5 mm length X 5 mm Width X 2 mm height). Later on there are two process parameters (laser power and scanning speed) considered Step 5, to prepare the sample with epoxy and resin. Step 6, to polish the sample in order to do the SEM and EDS. Step 7, to do the EDS and to check the elemental distribution in each sample and to do the SEM to check the microstructure of the optimized samples. Step 8, to do microhardness testing to figure out the hardness of each sample.

CHAPTER II

LITERATURE REVIEW

Ternary RMEA is composed of three refractory elements. Ternary RMEAs are intriguing for various reasons listed below. First, limiting the number of major elements simplifies the system while not sacrificing the mechanical properties. In its as-annealed condition, the quaternary TiZrHfNb (MEA) has σy of 879 MPa and an elongation of 15% (Y. Wu et al., 2014), which is equivalent to TiZrHfNbTa quinary alloy. The lack of Ta had no effect on the tensile qualities of the material. Similar results have been seen in the (FCC) HEAs: in the FeCoCrNiMn (Wu, Bei, Pharr, & George, 2014), the ternary CoCrNi MEA has the greatest σy, ductility, and fracture toughness (Gludovatz et al., 2016). The new Ti-Zr-Nb-Ta MEA has four times the ductility of the quinary equi-atomic Ti-Zr-Nb-Ta-Mo high entropy alloy (Nguyen et al., 2018). Second, the system's reduced number of constituent parts makes the thermodynamics and phase diagrams easier to grasp, as well as modeling studies on processes in general. Third, the ternary MEA would be more controllable than the counterpart higher-order system in terms of optimizing strength and ductility, particularly at high temperatures when precipitates and chemical order are involved. Fourth, restricting the number of participants may reduce the cost of some expensive materials as well as the difficulty of processing elements with considerable differences in melting temperatures and chemical affinity.

2.1 Application of MEA

The new material development which can sustain at extreme temperatures for high-temperature applications has become the focus of material scientists. In this respect, HEAs show a unique property and desirability for structural applications at high temperatures. Those unique properties, for instance, holding tensile strength at high temperatures, great thermal stability, significant fracture toughness at cryogenic temperature, and good wear and oxidation resistance (Cheng & Yeh, 2016; P. K. Huang, Yeh, Shun, & Chen, 2004; Miracle et al., 2014; Miracle & Senkov, 2017; Pickering & Jones, 2016; O. Senkov, Senkova, Dimiduk, Woodward, & Miracle, 2012).

In the aerospace sector, the alloy used to design components should be able to endure severe operating temperatures, creep, fatigue fracture development, cyclic and translational motions of parts at high speeds, and erosion. As a result, the components manufactured must be light, have strong high-temperature strength, fatigue, wear, and oxidation resistance, and be chemically resistant.

High operating temperatures can restrict the performance of turbine engines, making them more susceptible to creep, corrosion and fatigue failure. Ni-based superalloy is presently the most frequently utilized material for engine components at high temperatures (Essienubong, Ikechukwu, Ebunilo, & Ikpe, 2016). However, the hottest.

portions of advanced contemporary aero engines may develop temperatures up to 1600 0C, which is more than the melting point of Ni-based superalloys (1200–1300 C). Many research projects are being done to identify viable alternative materials to solve this restriction. For instance, Co-based

superalloy and refractory high entropy alloy (Perepezko, 2009). Additionally, some other refractory elements with Ni-based superalloy improve the high-temperature properties (Kaciulis et al., 2012; Tian, Liang, Li, Li, & Qian, 2011; W. Wang et al., 2008; A. Yeh & Tin, 2005).

Another leading-edge field is hypersonic vehicle applications, which operates in an ultra-high temperature environment (S. Gu & Olivier, 2020; J. Huang & Yao, 2020; Xie, Dong, & Jing, 2020). Traditional UTHMs may be classified into three categories [4]. The first category includes refractory metals including Nb, Ta, W, and Mo. The second is C/C composite materials, and the third is UTHCs (ultra-high-temperature ceramics), which are made up of metal borides, carbides, and oxides. Refractory metal materials have great mechanical characteristics at high temperatures and well-developed preparation procedures, but they are easily oxided at high temperatures, such as the Nb alloy, which would flake fast in a 400°C-air environment due to loose oxide layers [5]. Light, high mechanical properties, superior abrasion resistance, and other qualities make C/C composite materials useful in aerospace sectors. However, when C/C composite materials are exposed to 500°C air, the carbon components react quickly with oxygen in the air, resulting in fast oxidation failure and catastrophic structural damage [6]. In this regard, the ultra-high temperature ceramics can be a good replacement. Especially, refractory boride demonstrated remarkable resistance to oxidation at high temperatures [8-10]. Adding some additives such as Si may increase the oxidation resistance more. High entropy boride (HEB) possesses high mechanical properties at extreme high temperature [14]

2.2 The Microstructure of High and Medium Entropy Alloy

To describe the phase composition of the alloy microstructure, X-ray diffraction (XRD) investigation is commonly used. XRD data primarily provides information on material crystal structure. Body-centered cubic (bcc), face-centered cubic (fcc), hexagonal close packing (hcp), and other crystalline forms are common. A great deal of study has been done on the XRD system, and most material research now uses it to characterize the material.

Medium entropy alloy is another invented multi-component alloy, which is less complicated than high entropy alloy and gives good strength as well. He et al. (Q. He, Yoshida, Yasuda, & Tsuji, 2020) worked with Hf, Nb, Ta, Ti and Zr refractory elements and each time used four elements to make medium entropy alloy. The purpose was to check each elements impact on the microstructure and mechanical properties. After using vacuum arc melting process and then homogenization, there were three types of microstructures found: annealed grain (AG), granular morphology (GM) and dendritic morphology (DM). HCP elements (Hf,Ti,Zr) tended to disperse in the interdendritic zones, according to SEM-EDX data. The homogenization resulted in a considerable rise in AG while a significant drop in DM, indicating the eradication of dendritic segregation. Xu et al, (S.-P. Wang, Ma, & Xu, 2019) tried to check the Hf and Ti impact on the microstructure of the Nb-Ta solution. The chemical composition of HfNbTa and NbTa is consistent. Whereas TiNbTa showed dendritic microstructure. Additionally, lower melting temperature element Ti enriched at the inter-dendritic region and higher melting temperature Nb and Ta enriched at the dendritic region (S.-P. Wang et al., 2019).

2.3 The Mechanical Properties of Medium Entropy Alloy

HEAs and MEAs are valuable in both theoretical study and industrial production because of their unique microstructure and mechanical characteristics. Wang et al (X. F. Wang et al., 2021), prepared dual-phase refractory medium entropy alloy (RMEA) (Ti, Zr and Hf) ceramics by hot pressing. Where the flexural strength improved up to 2000^0C temperature due to lattice parameter mismatch. And the lattice parameter mismatch was attributed to the atomic radius variation among Ti, Zr and Hf. Because of its great comprehensive properties, the CrCoNi MEA is now a research hotspot. Gludovatz et al. (Raabe, Ponge, Dmitrieva, & Sander, 2009) investigated CrCoNi MEA at cryogenic temperatures and discovered that CrCoNi MEA outperformed all HEAs reported to date in terms of strength and damage tolerance. Zhang et al. (Z. Zhang et al., 2017) found CrCoNi MEA's outstanding strength, ductility, and toughness in their dislocation processes and 3D twin architectures. To improve the strength and ductility of Ti, Zr and Hf, Su et al, (Su et al., 2022) used transformation-induced plasticity (TRIP) and twinning-induced plasticity (TWIP). Tensile ductility is more critical for high-load applications than compressive ductility, however, RHEAs don't always have it. In this regard, Wang et al (S.-P. Wang et al., 2019), fabricated TiNbTa and HfNbTa by arc melting process which showed tensile ductility. Due to atomic parameters difference, the Hf showed better strengthening potency than Ti. Sometimes elemental combinations can impact the mechanical properties and microstructure. Five quaternary RMEA produced from Hf, Nb, Ti, Ta, Zr by vacuum arc melting process and then homogenized at Ar atmosphere. The ductility of HfNbTaTi, HfNbTiZr, HfTaTiZr, and NbTaTiZr alloys was much enhanced after homogenization, however th HfNbTaZr alloy displayed early brittle fracture. Homogenization of HfNbTaTi, HfNbTiZr, HfTaTiZr, and NbTaTiZr alloys resulted in the removal of inter-dendritic segregation and grain boundary precipitates, resulting in improved ductility (Q. He et al., 2020). Powder metallurgy was used to make NbTaTiV refractory medium entropy alloys,

hardness increased with the sintering temperature increasing from 1500 to 1700 C (W. Guo et al., 2019). With increasing the sintering temperature, segregation vanished, pore disappeared, a homogenous microstructure was created, and a 99.5 percent relative sintered density was attained. Adding Ti with NbMoTaW alloy improved the ductility (Han et al., 2018).

2.4 Selective Laser Melting Process & Processing Parameters

SLM is one of the additive manufacturing powder bed-based methods that fabricates a 3D component layer-by-layer utilizing a high-energy laser beam to selectively melt and consolidate tiny layers of metal powders. The powder layers usually have a thickness of 20–100 microns. Conventional technologies are incapable of producing complicated forms and ultrafine microstructures. Because fabrication procedures have a big role in determining microstructure, it's worth looking at different HEA manufacturing methods. AM technique allows for the production of complicated three-dimensional near-net shaped components without the use of dies, which is impossible to do with traditional methods (Chen et al., 2017). Components with basic geometry are popular in traditional manufacturing techniques to make them easier to manufacture. Typically, these designs aren't optimal for their intended use. Components may be created to the same functional specifications with fewer materials because to the geometric flexibility provided by SLM. Airbus announced a cabin bracket in 2014 [86] that was designed to save weight without losing functionality. Airbus hopes to employ metal additive manufacturing to make airplane components that are 30–55 percent lighter and consume 90 percent less raw material (Airbus, 2014). Metal AM's geometrical flexibility also enables the creation of lattice structures for weight reduction and the design of components for enhanced fluid dynamics. Croft Filters, for example, a custom filter producer, utilizes SLM to create innovative filters that only need one phase of manufacturing. Cutting, welding, and extensive labor operations are all part of the traditional filter

manufacturing process (Burns, 2014; Nickels, 2016). SLM may transform the manufacturing industry in terms of economics, in addition to the technical advantages of decreased tooling and design flexibility. Manufacturing may be decentralized because to advances in information technology and the internet. The economies of scale that high-volume, centralized production lines provide are diminished.

Processing factors such as laser power, scanning speed, hatch spacing and scanning strategy have a substantial impact on the product quality in the SLM process. Many scientific investigations (Attar et al., 2014; Attar et al., 2017; D. D. Gu, Meiners, Wissenbach, & Poprawe, 2012; Rao, Giet, Yang, Wu, & Davies, 2016; Zhou et al., 2017) discovered a substantial relationship between the microstructure and mechanical qualities of SLM printed parts and SLM method processing parameters. With the rapid movement of the laser beam, the temperature distribution in various locations of the powder bed varies rapidly, and it continues to alter across time and space (K. He & Zhao, 2018). Scan layers go through quick heat cycles during the SLM process. As a result of the temperature differential, residual stresses increase, and the printed object deforms unevenly (Kruth et al., 2004). To get the desired microstructure, characteristics, and densification, correct parameter selection is essential (Yanjin Lu et al., 2015; Xiong et al., 2019).

2.4.1 Laser Scanning Strategy

The number of studies on the scanning approach has expanded dramatically (Jia, Sun, Wang, Wu, & Wang, 2021). Optimizing the scanning strategy has been the subject of extensive study in order to enhance print quality. Lu et al. (Yanjin Lu et al., 2015) studied the microstructure and characteristics of SLM-printed Inconel-718 alloy using a scanning approach with varying island sizes. Larger island samples encountered greater residual stresses as the density of manufactured samples rose. They discovered that a sample with a 55 mm^2 scanning method was

ideal for their intended use after examining the relative density, residual stress, and mechanical characteristics of the samples.

Ramos et al. (Ramos, Belblidia, & Sienz, 2019) experimented with scanning pathways that were unidirectional, zigzag, and alternate. The heat was more uniformly distributed across the layer due to the scan sequence in the alternating scanning technique, resulting in symmetric deformation, whereas the other two procedures generated asymmetric deformation. In comparison to unidirectional and zigzag techniques, the alternating strategy may minimize printed component deformation by 18.4% and 9.3%, respectively. While sweeping scanning direction had no influence on residual stresses, Zou et al. (Zou et al., 2020) found that altering the scanning sequence might dramatically reduce residual stress on a component when compared to unidirectional and alternating scanning procedures. The residual stress was very low in the first sweep due to large hatch spacing.

2.4.2 Scanning Direction:

Scan direction plays an important part in SLM's ability to produce high-quality products. Wang et al. (L. Wang et al., 2018) used two scanning techniques to create SLM AlSi10Mg parts: a) horizontal sequential pattern in which the laser moves in the X-direction, b) descending sequential pattern in which the laser moves at an angle to the X-direction. They compared the residual stresses formed in the X and Y directions for both patterns and discovered that the horizontal sequential pattern yielded parts with significantly lower residual stresses in both directions.

Trosch et al. (Trosch, Strößner, Völkl, & Glatzel, 2016) created their samples with three scanning orientations: horizontal, vertical, and 45° to investigate the influence of scanning direction rotation on the mechanical characteristics of Inconel 718. They discovered that

horizontally constructed specimens had the highest average tensile strength, whereas specimens rotated 45 degrees had the lowest. In a study by Guo et al. (L. Guo et al., 2021), the scanning rotation method was found to have an influence on cracking. They used two scanning rotations of 45° and 67° to make FeCoCrNiMn HEA. In comparison to the 67-scanning rotation technique, they discovered that 45° scanning rotation formed microstructures with dominating epitaxial development of columnar dendrites.

2.4.3 Hatch Spacing

Hatch spacing has a significant impact on the quality of 3D-printed parts. For producing 3D samples with good relative densities and acceptable surface smoothness, proper hatch spacing is critical (Dong, Liu, Wen, Ge, & Liang, 2019). The hatch spacing, which affects grain size and morphology, determines the remelting area of neighboring tracks (Carter, Martin, Withers, & Attallah, 2014; Sateesh, Kumar, Prasad, Srinivasa, & Vinod, 2014). Increasing hatch spaces reduces the overlap between two successive scan tracks, and more porosity develops, resulting in reduced density and a rough surface throughout the SLM process. Lower scan spacing, independent of power or scanning speed, produced smooth surfaces, according to Pupo et al, (Pupo, Delgado, Serenó, & Ciurana, 2013). They tested several scan spaces and discovered that a lower scan space value produced the greatest results in terms of surface smoothness owing to the heat buildup effect. Lower scan spacing caused heat to accumulate from the preceding track to the scanned track next to it. This technique sped up the cooling of the scanned track and made it easier to produce a continuous layer with enough overlap. Enneti et al, (Enneti, Morgan, & Atre, 2018) investigated the hatch spacing and scanning speed impact on the densification of tungsten while layer thickness and power were kept constant. The densification increased with increasing the energy density.

2.4.4 Scan Vector Length:

In the SLM process, the scanning vector length is critical. During scanning with a lengthy scan vector, a larger amount of the heat collected in the melt pool can readily disperse to the environment via convection, preventing the neighboring track from melting. As a result, a bigger scan vector causes the melt pool to cool faster and the average surface temperature to drop. A shorter scan duration, on the other hand, allows for greater temperatures in the melt pool's nearby region and encourages more even temperature distribution throughout the created surface. When a short scan vector is utilized, the period between two subsequent track melting is very short, and heat from a melt pool does not have enough time to disperse away. Instead, the majority of the heat is spread among the melted tracks, which aids in raising the total surface temperature. Higher surface temperatures reduce temperature gradients, thermal expansion mismatches, and cooling rates in the melt pool region, resulting in lower residual stresses.

Interlayer rotation between subsequent layers, in which the heat flow direction is rotated, is more useful for achieving a uniform temperature distribution (Amirjan & Sakiani, 2019). Shorter scan vector lengths are often better for reducing residual stress and improving the mechanical properties of AM products (M. Guo, Ye, Jiang, & Wang, 2019; Zaeh & Branner, 2010). Part deformation, failure, and cracking of the recoating blade are caused by excessive residual stress. The residual stress in a 3D object manufactured by selective laser melting should be small. Shorter scan lengths have been shown in studies to help reduce residual tensions (Promoppatum & Yao, 2020).

Below are the different parameters considered for the refractory metal fabricated by SLM.

Material	Laser Power	Velocity (mm/s)	Hatch distance (micron)	Layer thickness (Micron)	Energy Density	Reference paper
NbMoTaW		250	0.1	100	0.943 J/mm,	(H. Zhang et al., 2019)

WTaMoNb	400	250	0.1	100		(H. Zhang, Xu, Xu, Lu, & Li, 2018)
W powder	250-380	200-600		30		(Ren, Liu, Lu, Huang, & Yi, 2021)
Mo-Alloy	310-450	200-1000		50	900-160 J/mm^3	(Z. Guo, Wang, Wang, Ding, & Liu, 2020)
WMoTaNbV	200,600	100,800	0.045, 0.12	50		(Huber et al., 2021)
W powder	250,450	200,500				(Meng Guo et al., 2019)
W heavy Alloy	(50–350)	100-600				(Iveković, Montero-Sistiaga, Vanmeensel, Kruth, & Vleugels, 2019)
NbMoTaX	300	300	0.06	30		(H. Zhang et al., 2021)
WMoTaTi	320,360	300,400,500	0.08, 0.10,0.12	30	177-444 J/mm^3	(C. Liu et al., 2022)
W powder	90	200-1400	0.015, 0.03	30	1000 J/mm3	(Enneti et al., 2018)

CHAPTER III

METHODOLOGY

3.1 Materials Selection

The WMoTi MEA will be produced using 99.5% pure W,Mo and Ti elemental powders. All the

physical details of all the elemental powders are provided in Table 2.

Table 2 Physical properties of elemental metal powder.

Properties	Tungsten	Molybdenum	Titanium
Atomic number	74	42	22
Atomic weight (gm)	183.85	95.94	47.87
Melting point (^{0}C)	3,410 °C	2625°C	1668 °C
Boiling point (^{0}C)	5,660 °C	4639 °C	3287 °C
Density (g/cm^3)	19.3 grams/cm3	10.3 g/cm³	4.5 g/cm³
Supplier Company	Tekna	Tekna	LTW
Purity (%)	99.90%	99.90%	99.90%
Particle Size (μm)	<45	<45	<45
Powder Morphology (shape)	Spherical	Spherical	Spherical

Tungsten and Molybdenum powder was purchased from Tekna supplier and Titanium powder was

purchased from LTW supplier. The shape of the powder is observed by SEM machine. And the

picture is attached below. Figures 4, 5 and 6 are showing that in 150X magnification, all the powders are showing a spherical shape.
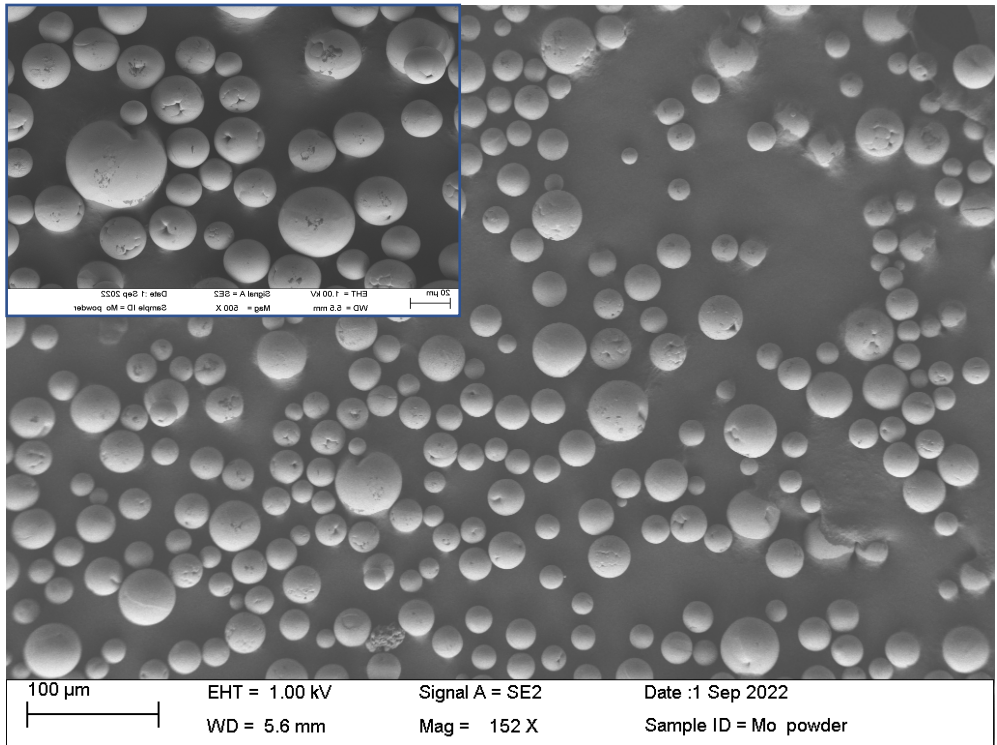
Figure 2: SEM picture of elemental Molybdenum powder.

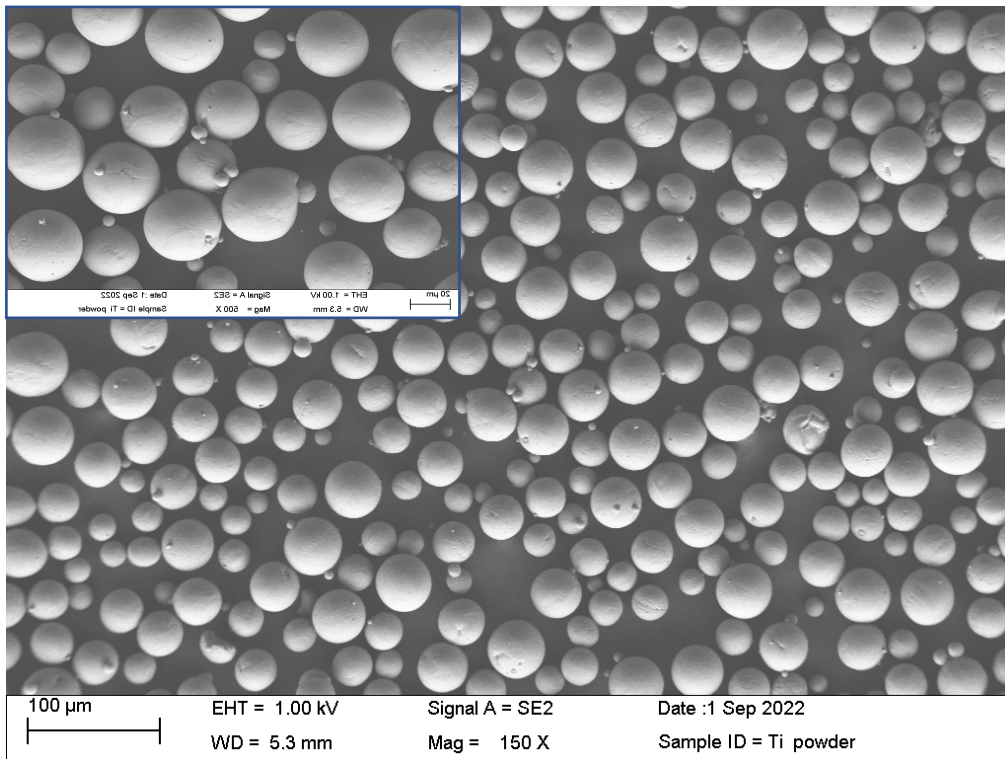Figure 3: SEM picture of elemental Titanium powder.
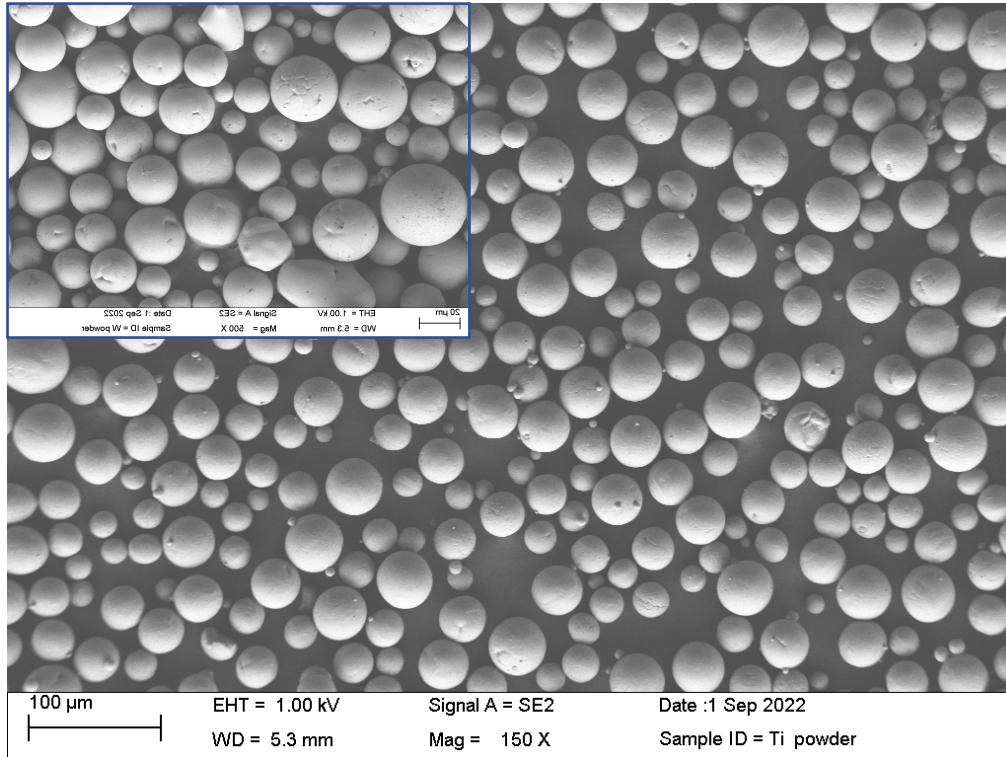
Figure 4: SEM picture of elemental Tungsten powder.

3.2 Powder Composition and Mixing

Elemental powders were mixed manually. The nominal composition of different metals in the WMoTi MEA samples are given in Table 2. For getting a homogeneous mixture, the mixed powder will be placed on a V-type blender (figure 7) and rotated for 18 hours at 25 rpm.

Table 3 Powder composition of WMoTi alloy.

	W	Mo	Ti
Weight %	29.28%	56.10%	14.62%
Molar Ratio	0.33	0.33	0.33

Figure 5: V-Type Blender to mix the powder.

3.3 AM Fabrication

3.3.1 2 X 2 X 2 Test Series of WMoTi (Test 1):

To investigate the different process parameters on the microstructure and the diffusion process, 8 blocks were printed with different laser power, hatch distances and scanning speeds. 2 different laser power, scanning speed and hatch distances were considered. Each block was 10mm x 10mm. The printing was done for 10 layers. Table 4 is showing the process parameters. The energy density is calculated by the below equations.

Energy density $= (P)/(v \times h \times l)$

Here,

P = Laser power

v = Scanning speed

h = Hatch spacing

l = Layer thickness.

Table 4 Test 1 design parameters

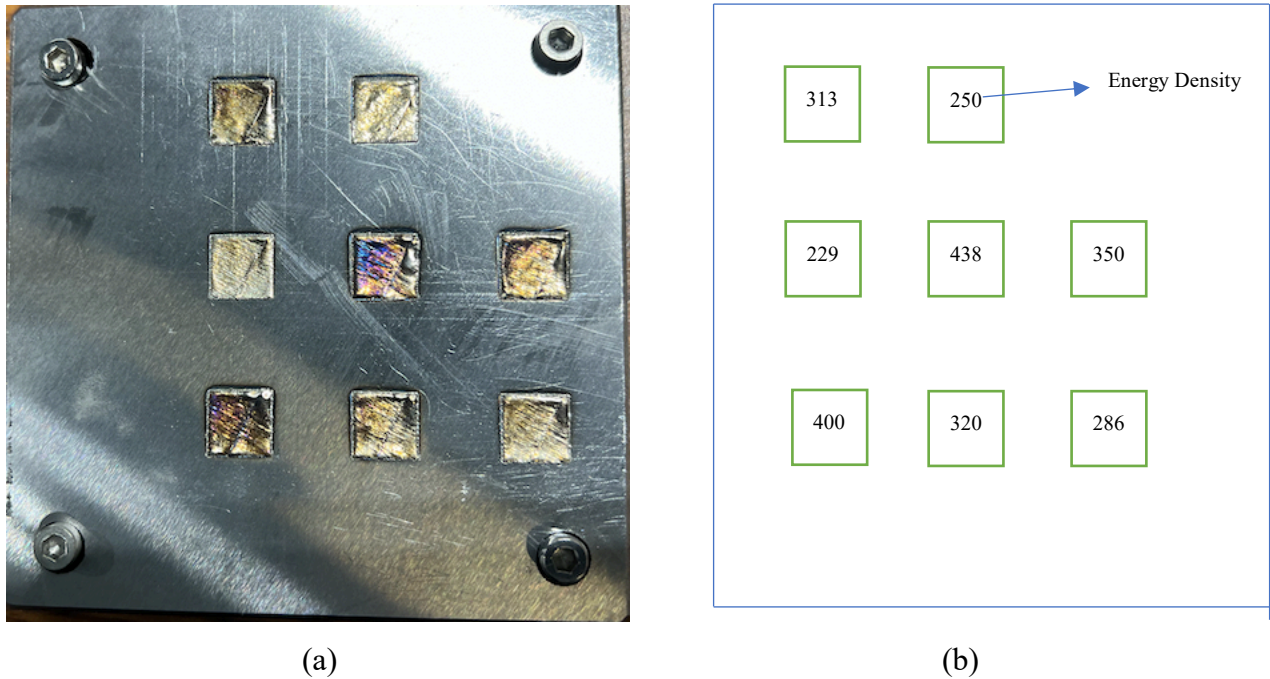| Test 1					
Run	Laser power (W)	Scanning Speed (mm/s)	Hatch distance (mm)	Energy Density (J/mm^3)	Layer thickness (mm)
1	320	250	0.08	400	0.04
2	320	250	0.1	320	0.04
3	320	350	0.08	286	0.04
4	320	350	0.1	229	0.04
5	350	250	0.08	438	0.04
6	350	250	0.1	350	0.04
7	350	350	0.08	313	0.04
8	350	350	0.1	250	0.04

Figure 6: (a) Test 1 Printed Samples (10mm X 10mm). (b) Designed samples with energy density

The SLM process started with the machine preparation. Cleaning the machine in order to avoid contamination. Pour the mixed powder into the dispenser Then balanced the gap between the recoater and the build plate. Steel substrate has been used for the build plate. Made the first layer by trial and error on the build plate. Preheat the substrate up to 80^0C. Cleaned the lens. Closed the chamber and opened the argon tank to flow the argon gas. Then stored the designed sample in the EOS M290 machine through EOSPRINT software. Started the building task. The machine started to clear the filter by itself. And the targeted oxygen level was 500 parts per million. When the machine is prepared to print then printing started. The recoater blade started to wipe the powder from the dispenser to the build plate and the laser started to melt the powder. After 10 layers, the

recoater blade started crushing the sample, as the sample was wrapped. Immediately the printing was stopped and the build plate was taken out after proper cooling.

### 3.3.2 2 X 2 X 2 Test Series of WMoTi (Test 2):

Test 2 was conducted by reducing the energy density. Table 5 is showing the different parameters. The sample size was also reduced from 10 mm to 5 mm this time in order to cut the sample easily. The design orientation was also changed so that the powder flow can be ensured uniformly.

Table 4 Test 2 design parameter

TEST 2					
Run	Laser power (W)	Scanning Speed (mm/s)	Hatch distance (mm)	Energy Density (J/mm^3)	Layer thickness (mm)
1	320	450	0.08	222	0.04
2	320	450	0.1	178	0.04
3	320	400	0.1	200	0.04
4	320	350	0.1	229	0.04
5	350	450	0.08	243	0.04
6	350	450	0.1	194	0.04
7	350	400	0.1	219	0.04
8	350	350	0.1	250	0.04
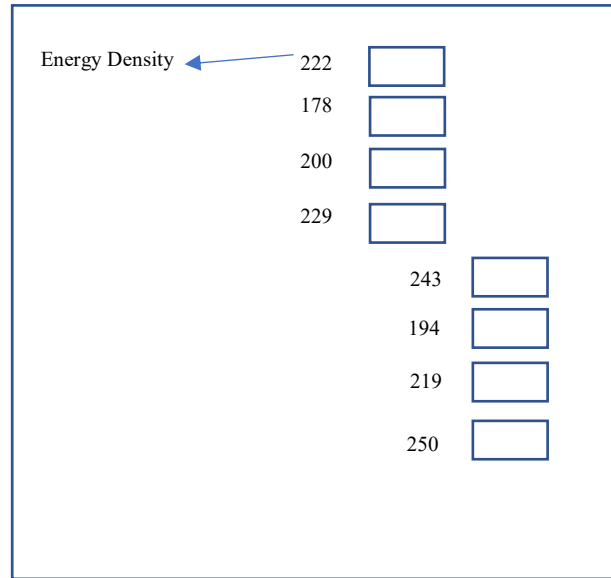
Figure 7: (a) Test 2 Printed Samples (10mm X 5mm). (b) Designed samples with energy density

The SLM machine was prepared as like as the earlier way. The printing was successful up to the 14 layers. Then from 14 layers to 17 layers there were overburn and recoater blade was crushing with the sample. At that point the printing was stopped and the sample was taken out.

3.3.3 2 X 2 X 2 Test Series of WMoTi (Test 3):

In test 2, the sample was ok up to 14 layers. After that it over burnt. So in this test we kept the same energy density up to 10 layers and then the energy density reduced from 11 layers. Each sample size has been reduced in size from 10 X 5 mm to 5 X 5 mm. Table 6 is showing the new parameters executed from layer 11. This was successful up to layer 17. Then the samples over burnt. Additionally, the recoater blade was crushing the samples. The machine was prepared the same way as like earlier.

Table 5 Test 3 design parameters

Run	Laser power (W)	Scanning Speed (mm/s)	Hatch distance (mm)	Energy Density (J/mm^3)	Layer thickness (mm)
1	220	450	0.08	153	0.04
2	220	450	0.1	122	0.04
3	220	400	0.1	138	0.04
4	220	350	0.1	157	0.04
5	200	450	0.08	139	0.04
6	200	450	0.1	111	0.04
7	200	400	0.1	125	0.04
8	200	350	0.1	143	0.04
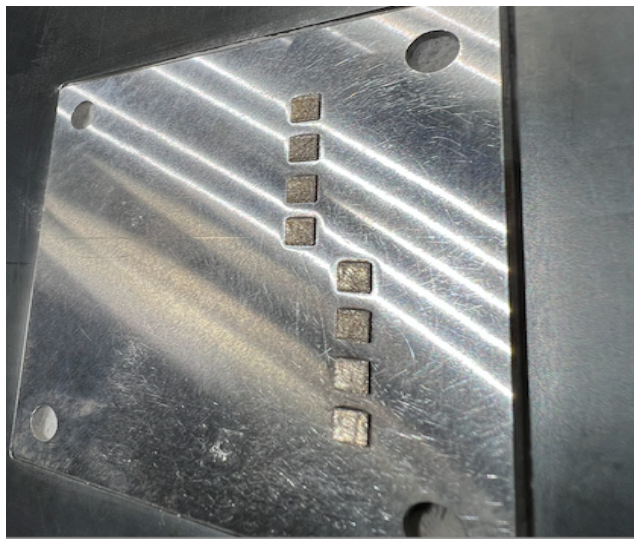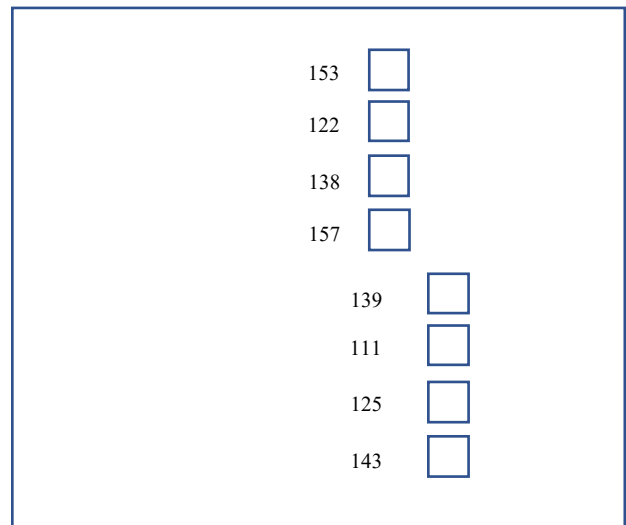
(a)   (b)

Figure 8: (a) Test 3 Printed Samples (5mm X 5mm). (b) Designed samples with energy density

3.3.4 2 X 2 X 2 Test Series of WMoTi (Test 4):

In test 4 the layer thinness has been increased from 40 to 80 microns. The first 10 layers were based on test 2 parameters and then the rest layers parameters were based on table 8. The machine was prepared as like the earlier steps described. The printing was successful for 17 layers

and the recoater blade started crushing the sample. As a result, after 17 layers the printing as stopped.

Table 6 Test 4 Design Parameters

Run	Laser power (W)	Scanning Speed (mm/s)	Hatch distance (mm)	Energy Density (J/mm^3)	Layer thickness (mm)
1	200	450	0.08	69	0.08
2	200	450	0.1	56	0.08
3	200	400	0.1	63	0.08
4	200	350	0.1	71	0.08
5	220	450	0.08	76	0.08
6	220	450	0.1	61	0.08
7	220	400	0.1	69	0.08
8	220	350	0.1	79	0.08

3.3.5 2 X 2 Test Series of WMoTi (Test 5):

Test 5 is done with the new Ti substrate. High-Strength Grade 5 Titanium Bar, 1/4" Thick x 1" Wide x 1/2 Feet Long titanium bar is purchased from McMaster-Carr. Cutting titanium bar is very difficult. Water jet cutting system has been used to cut the titanium bar. This cutting system is installed at outside UTRGV, and the name of the shop is Amida machine shop. Titanium bar

was cut into 3 pieces. Each 1/4" Thick x 1" Wide x 2" Long. Aluminum reduced build substrate was machined in order to put the one piece of titanium. Figure 11 is showing the new Ti-substrate.
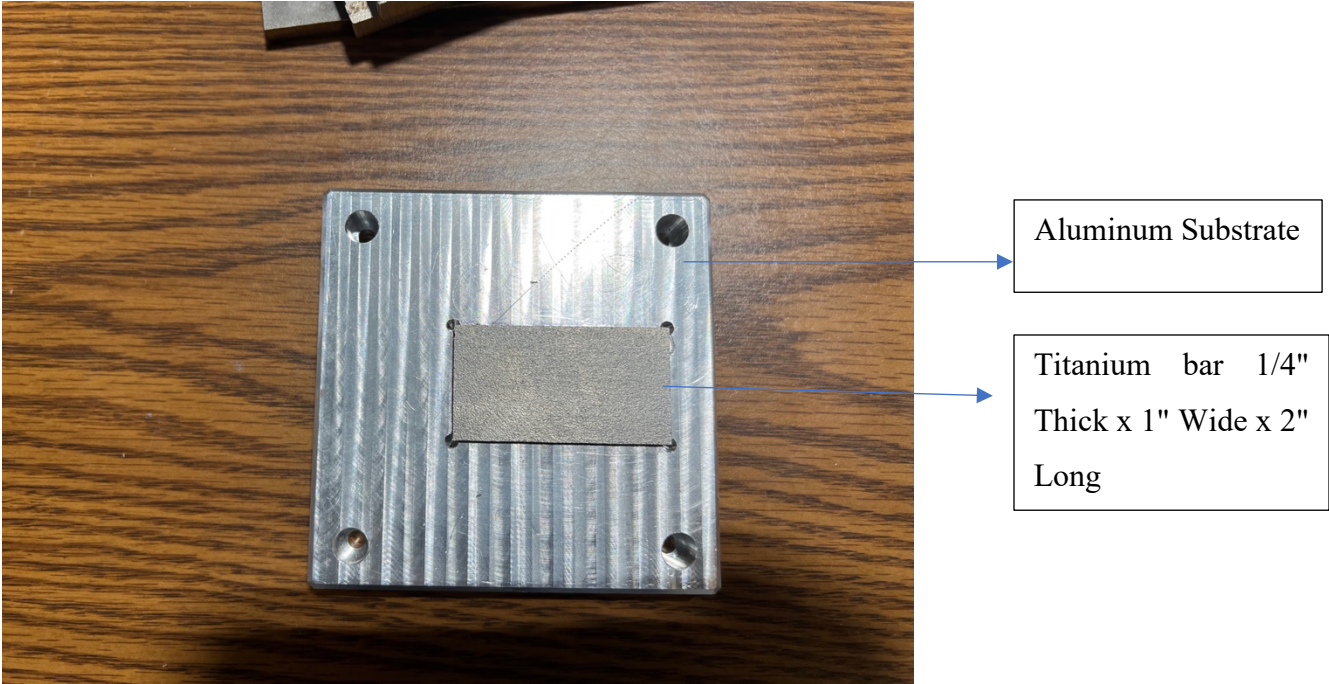

Figure 9: New Ti Substrate

The position of the samples changed. The designed and printed samples are showing in figure 12. This time machine was prepared as like earlier. The printing was successfully done and completed. Laser power and scanning speed were changed. Laser powers were 350 and 280. The scanning speed was considered 380 and 250. The layer thickness and hatch distance were considered constant. The whole parameter is shown in table 8.

Table 7 Test 5 Design Parameters

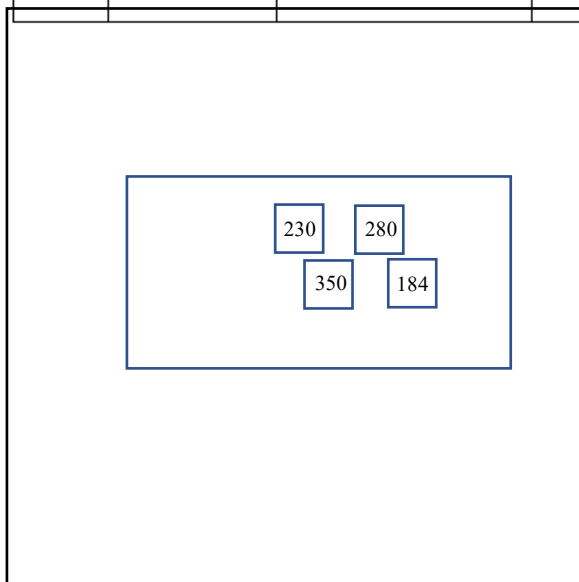| Test 5	Titanium Bar				
Run	Laser power (W)	Scanning Speed (mm/s)	Hatch distance (mm)	Energy Density (J/mm^3)	Layer thickness (mm)
1	350	380	0.1	230	0.04
2	280	250	0.1	280	0.04
3	350	250	0.1	350	0.04
4	280	380	0.1	184	0.04

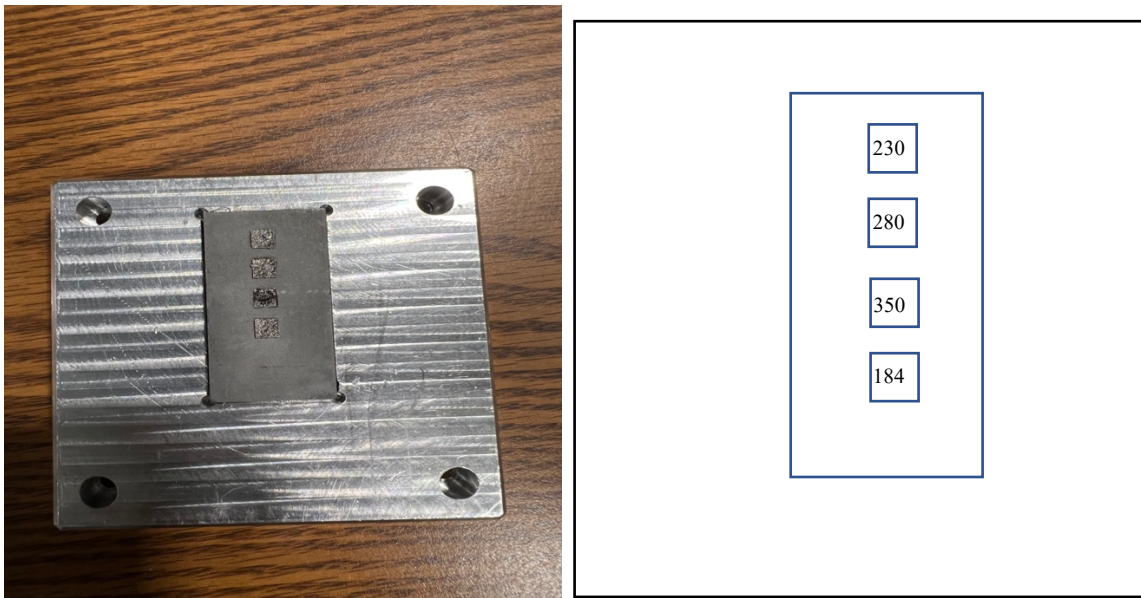Figure 10: Designed samples with energy density

3.3.6 2 X 2 Test Series of TiWMo (Test 6):

From test 5, the issue was identified as lots of unmelted tungsten. To check how the TiWMo alloy reacts with the tungsten substrate, test 6 was designed with the same parameters as like test 5. The machine was prepared as like test 5.

The design of the sample has been changed. The sample position was kept in one column in order to achieve uniform powder distribution. The printing failed after 8 layers.

Table 8: Test 6 Design Parameter

Test 5	Tungsten Bar				
Run	Laser power (W)	Scanning Speed (mm/s)	Hatch distance (mm)	Energy Density (J/mm^3)	Layer thickness (mm)
1	350	380	0.1	230	0.04
2	280	250	0.1	280	0.04
3	350	250	0.1	350	0.04
4	280	380	0.1	184	0.04

(a)

(b)

Figure 11: (a) Test 6 Printed Samples (5mm X 5mm). (b) Designed samples with energy density

3.4 Polishing and Sample Preparation

After the 7 tests, the samples were prepared for the SEM test. There were 3 samples picked for the first polishing and sample preparation. Then took 3 parts of acrylic powder with 2 parts of hardener by volume. Mixed them well. Poured into the mold where the samples were placed. After pouring the mixer, the holder was kept for 24 hours at room temperature to cure. The sample is

ready to polish. The polishing was done in the materials lab. There were four different grit papers. After grinding in all the grip papers then sample were taken to the coarse and then fine polished machine.

3.5 Testing

To check the morphology and microstructure of the sample Scanning Electron Microscope (SEM) machine was used. The magnification was used from 50X, 250X and 500X. To check the composition ratio Electron Dispersive X-Ray Spectroscopy (EDS) was used. To measure the microhardness, Vicker microhardness testing machine was used. Normal microscope machine was used to check the polished surface. Microhardness was measured by the Vickers hardness testing machine in the materials lab. Before measuring the hardness, the sample was polished with four different grit papers for 40 minutes. After that, the sample is taken to the coarse and fine diamond disk for another 40 minutes.

CHAPTER IV

RESULT AND DISCUSSION

4.1 Powder Flowability Test

Powder flowability is very important in the powder bed fusion additive manufacturing process. The angle of repose was found 24.90 degrees for equiatomic WMoTi alloy. Figure 14 is showing the result.
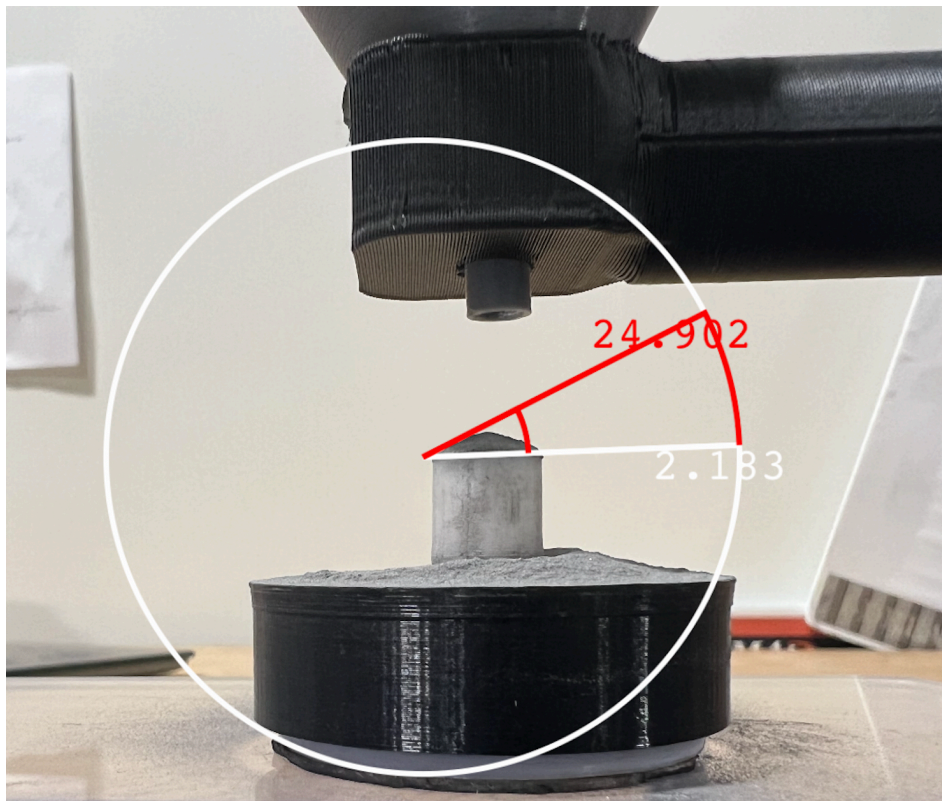

Figure 12: Angles of Repose for WMoTi alloy.

Table 9 is presenting the classification of the flowability. Based on the data TiWMo alloy possess very free flowability.

Table 9: Classification of flowability based on angles of repose (Zegzulka, Gelnar, Jezerska, Prokes, & Rozbroj, 2020)

Angle of Repose, α (AOR)	$20° < α < 30°$	$30° < α < 38°$	$38° < α < 45°$	$45° < α < 55°$	$55° < α < 70°$
Flow properties	Very free-flowing	Free-flowing	Fair to passable flow	Cohesive	Very cohesive

4.2 Design of Experiment for test 1 – test 4

Refractory and hard materials have diversified melting temperatures. In order to have proper diffusion, melting and bonding between the elements, choosing the right parameters is very important and critical. Many papers have analyzed the process parameter's effect on the microstructure and phase of refractory metals. For tungsten and molybdenum alloy, the optimized energy density is found between $250 – 400$ J/mm^3 (Z. Guo et al., 2020; Iveković et al., 2019; Ren et al., 2021). As a result, the initial energy density range is considered between $250 – 400$ J/mm^3 in test 1. The measurement of each small cube was 10 mm X 10 mm. It was observed from figure 8, the higher energy density burnt the sample. Each of the sample's surfaces is distorted as well. In compare with 8 samples, the lowest energy density showed a better surface finish visually. Test 2 was launched with the reduced energy density and after 12 layers the printing failed again. From figure 9, it's visible that the samples are over burnt. Therefore, the subsequent test 3 and test 4 proceeded with less energy density. Table 4-7 represents the data. To do the further analysis, three samples were taken for the SEM and EDS analysis.

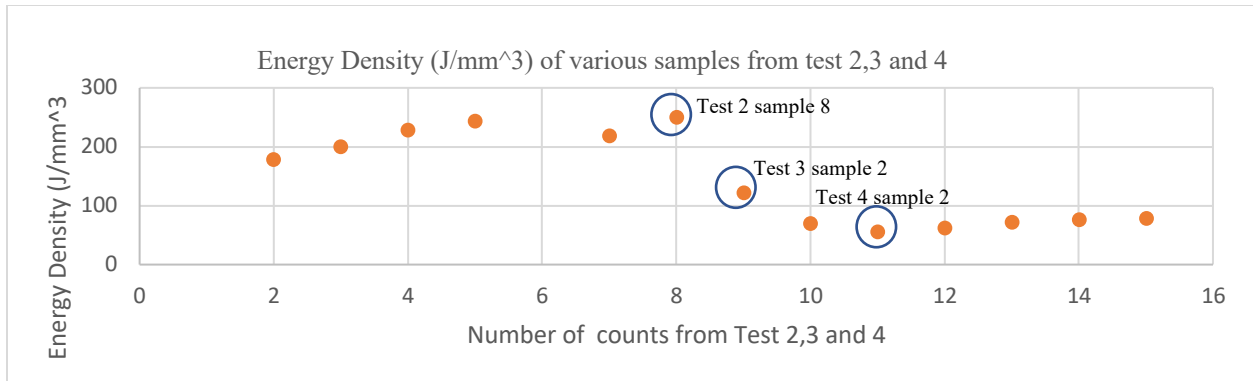Figure 15 is representing the energy density for different samples from test 2 to test 4.

Figure 13: Samples from tests 2-4 with different energy densities.

Among 15 counts, 8, 9 and 11 was picked to check the SEM and EDS. As those samples were representing high, medium and low energy densities.

4.3 Microstructure and EDS Analysis of TiWMo on Steel Substrate

Figure 16 is showing the SEM pictures of three samples in different magnifications.
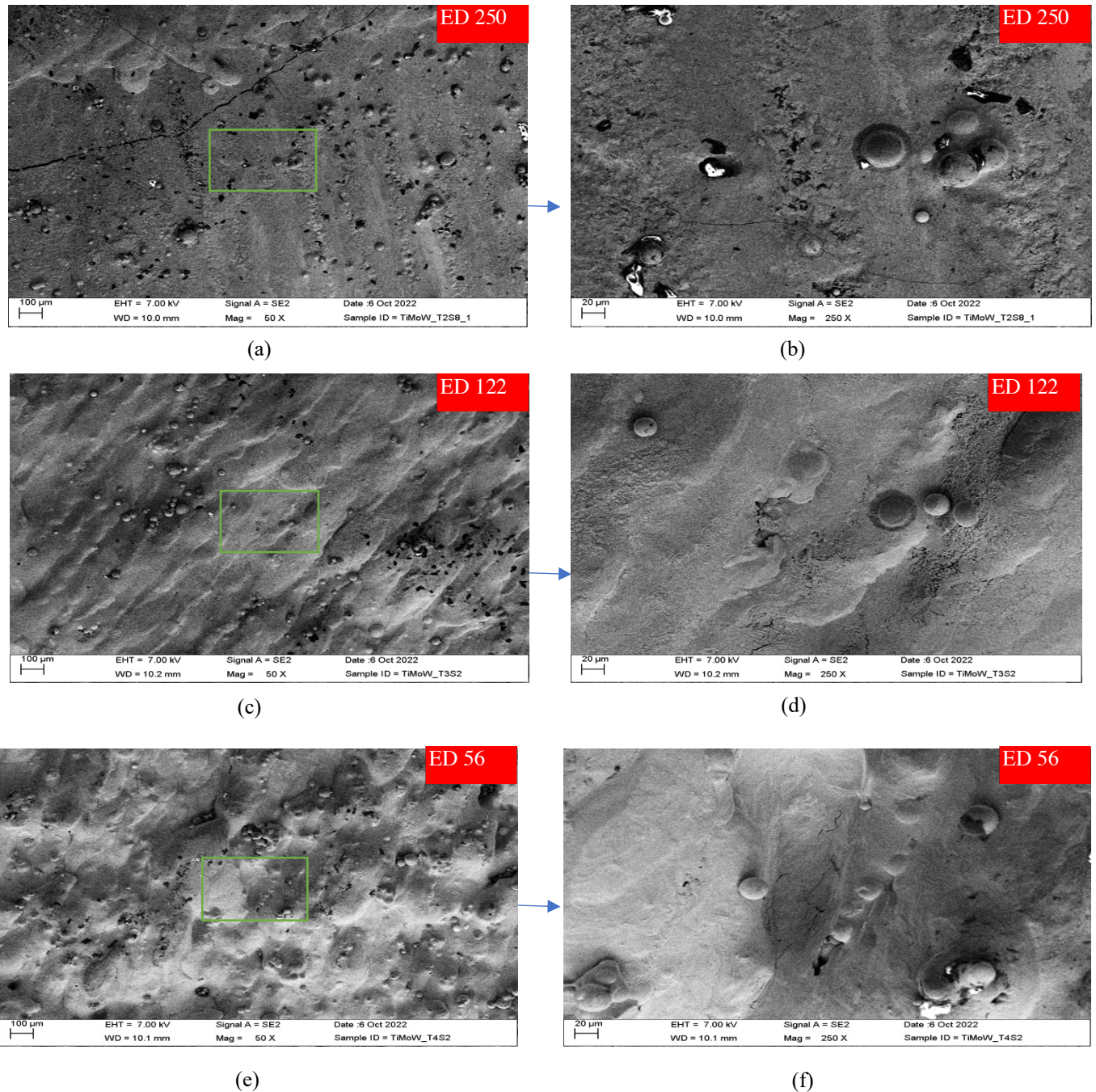

Figure 14: SEM pictures of three samples into different magnification. (a) & (b) test 2 sample 8, (c) & (d) test 3 sample 2, (e) & (f) test 4 sample 2.

Pictures were taken from the top surface without polishing. Pictures (a) to (f) show lots of unmelted particles attached to the surface. At high energy density, the crack is visible in picture (a). At

medium energy density (c), the laser track is visible. All the pictures are showing different brightness.

EDS analysis is showing two important findings in figure 18. The titanium atomic ratio is 60-80% in each of the samples. Whereas the expected ratio is supposed to be 34%. Additionally, the presence of Fe in the sample. Fe is reactive with Ti. Titanium mixed with Fe form TiFe and Fe_2Ti phases (Louzguine-Luzgin, 2018). Both phases are brittle in nature (Mo et al., 2018). EDS analysis points the higher Ti ratio at the surface of the sample. Through the cross-section, getting more Fe elements is more obvious. For better build quality and to print successfully, mixing powder properly and reducing the Fe reaction with other elements is very important and critical. Fabricating TiWMo medium entropy alloy in titanium substrate is necessary in order to avoid any
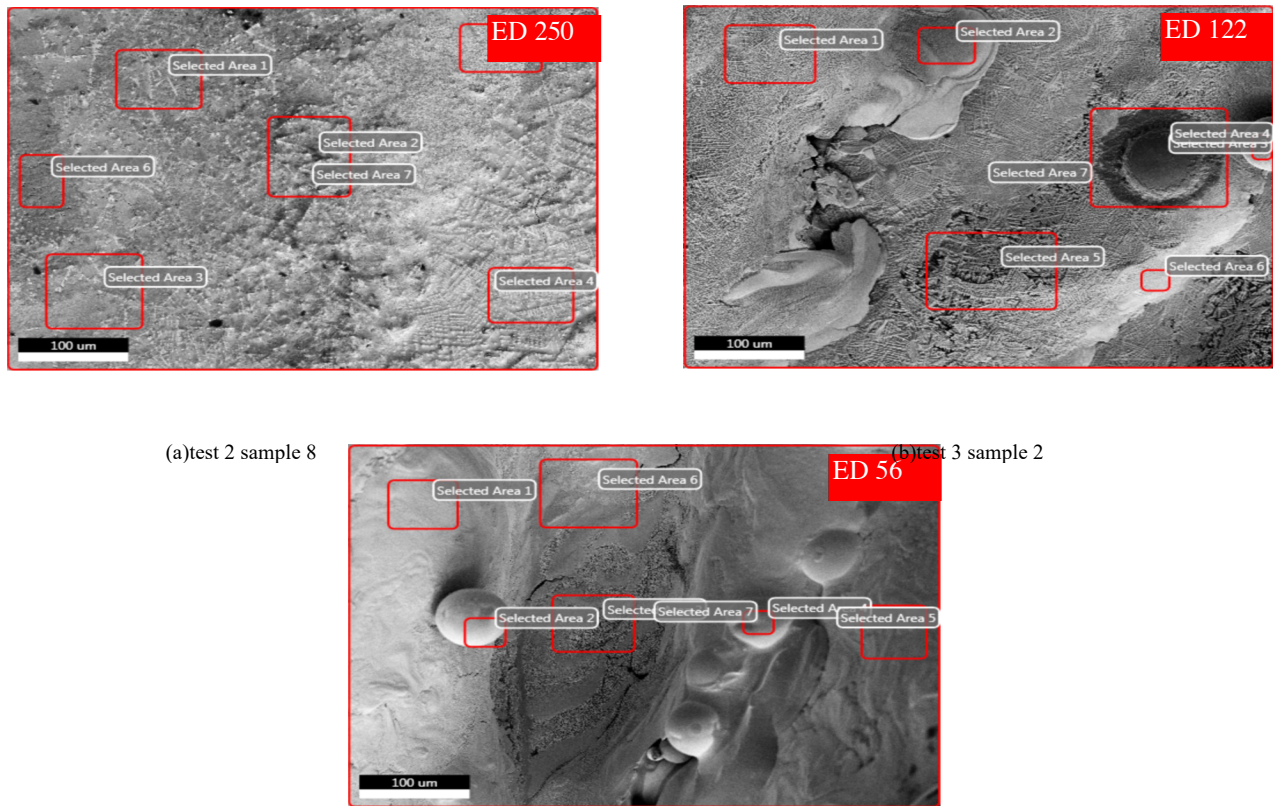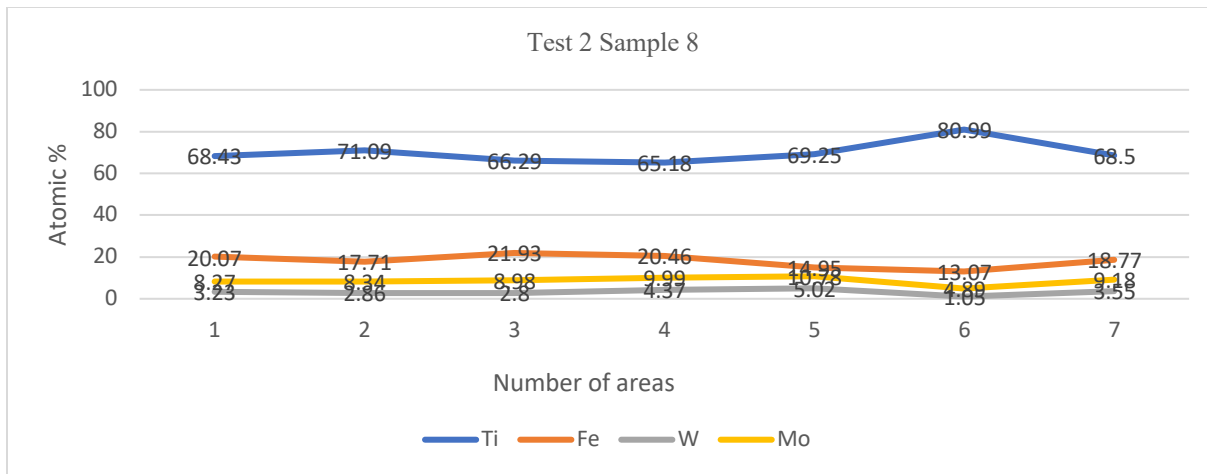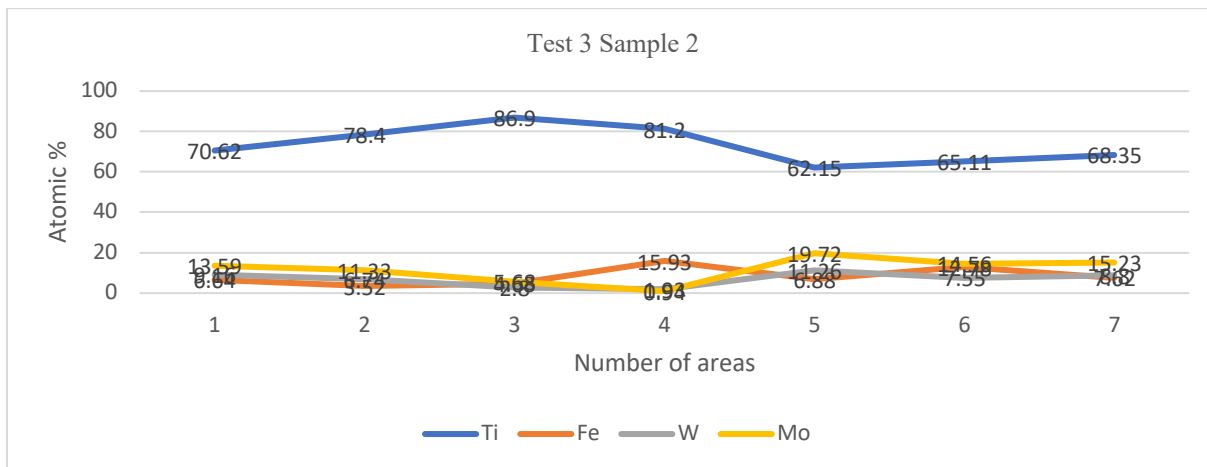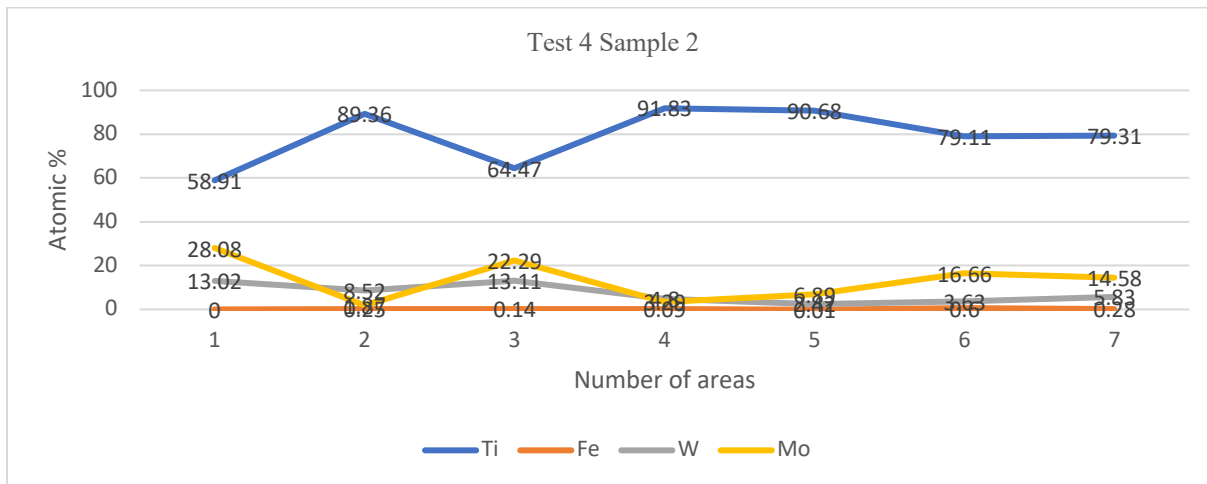

(a)test 2 sample 8   (b)test 3 sample 2

Figure 15: SEM picture in higher maginification for (a)test 2 sample 8, (b)test 3 sample 2 (c)test 4 sample 2

(a)

(b)

(c)

Figure 16: EDS analysis of three samples (a) test 2 sample 8, (b) test 3 sample 2 and (c) test 4 sample 2.

4.4 Effect of Process Parameters of TiWMo on Titanium Substrate

Comparative studies were created and carried out to investigate the impact of processing parameters on the microstructure of TiWMo RMEA sections. In figure 19, the green rectangle in each sample was considered the area to calculate the surface porosity. This surface was taken from the cross-section of the each sample. ImageJ software was used to calculate the area of each pore. It is observed that, with increasing laser energy density the pores
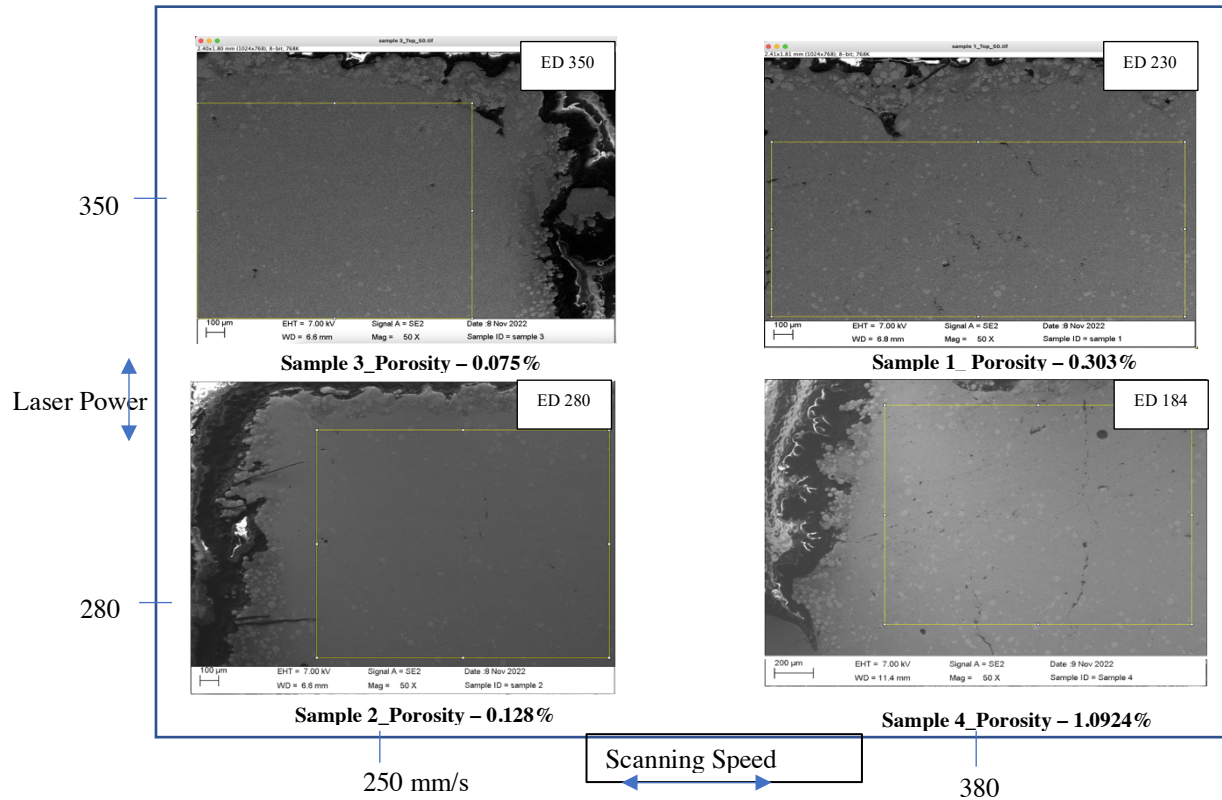

Figure 17 : Impact of the process parameters on the surface porosity of TiWMo RMEA

and microcracks were reduced. Since the extraordinarily high melting temperatures of these components in RMEA, partial melting of powders might prevent proper fusion due to insufficient laser power or energy density. Additionally, from the powder mixing to the print, all the process

was done in an open environment, therefore the oxygen could contaminate the powder. Which might be another reason of having pores and cracks.

4.5 Microstructure and EDS Analysis of TiWMo on Titanium Substrate

To avoid contamination from the substrate, now titanium substrate was made and printed the samples on it. Test 5 was done by changing the laser power and scanning speed. Figure 20 is showing the four samples made by different process parameters. The building direction is from
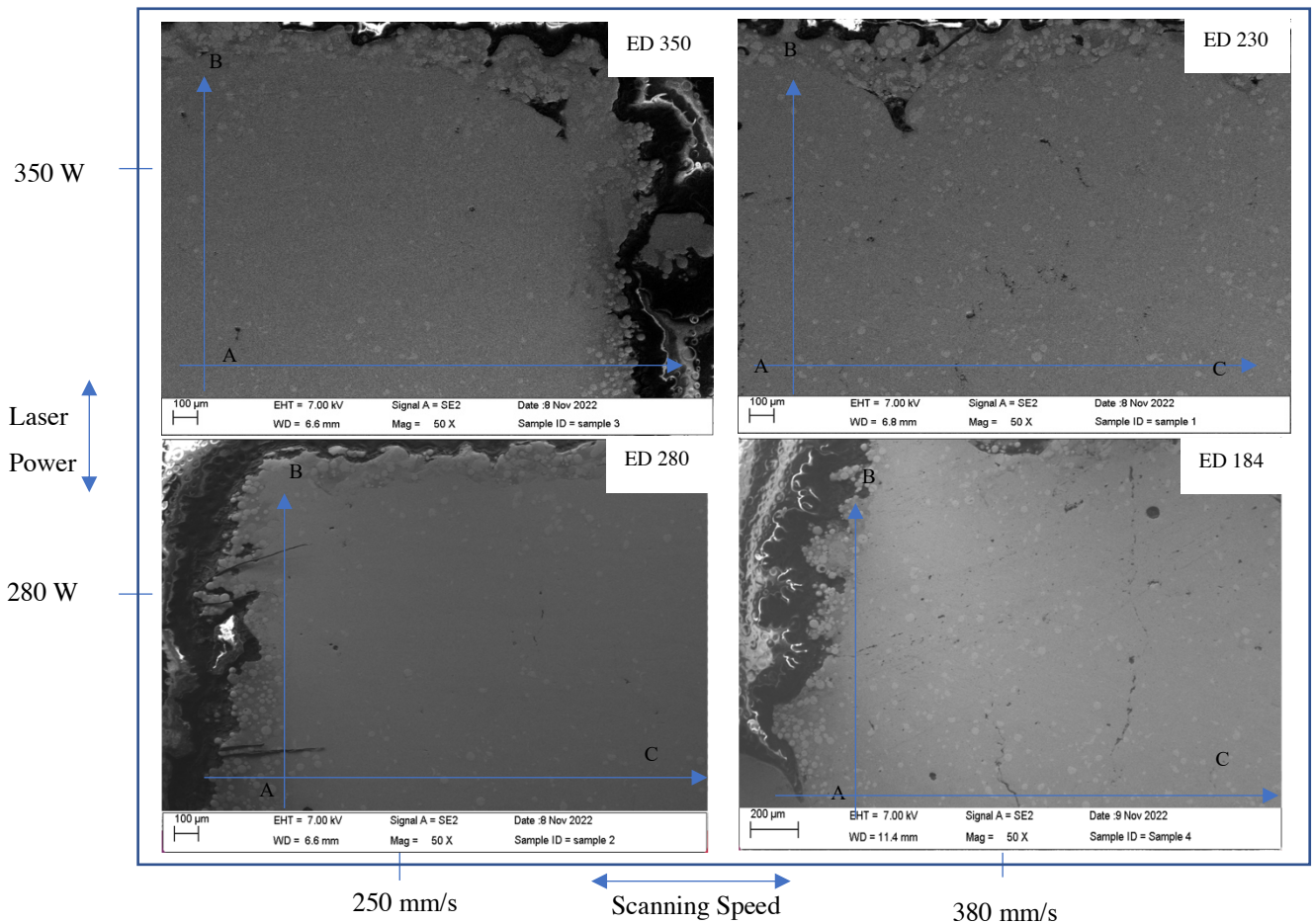
Figure 18: SEM pictures of four samples in different process parameters.

A to B. AC is representing the bottom layer of the each sample. Additionally, the SEM is done through the cross-section of the samples. All the pictures can be divided into two sections. One is there is no contrast and in the second section, there are lots of small particle size bright areas. Figure 21 is showing the EDS analysis of samples 1 and 3 in higher magnification. Images (a) and

(b) is the SEM images of sample 3 and 1 respectively in higher magnification. In fig 21 (a), 4 different areas were selected to check the composition. Fig 21 (c) is representing stable composition in all the four different areas. The average Ti is 40.5%, W is 17% and Mo is 32.6%. As a result, it could be anticipated that the tungsten, molybdenum and titanium atoms interacted with each other and formed a uniform random solid solution. In figure 21 (b) sample 1, there are 6 different areas are considered to study the composition. Bright areas are 3,4 ad 6. Picture 21 (d) depicts that tungsten is 80.78%, 77.63% and 81.55% respectively. Therefore the bright regios are representing unmelted tungsten particles. In the other regions 1,2 and 5 the atomic ratios of the elements are homogenous. The average Ti is 44.06%, Wis 22.56% and Mo is 33.28%. Molybdenum is more stable and closer to the expected atomic percentage.
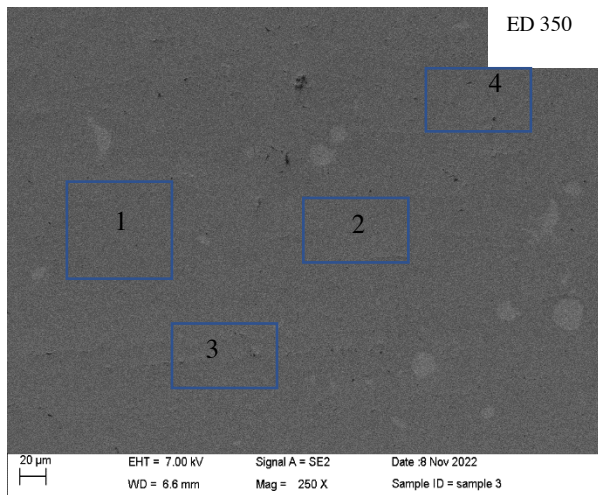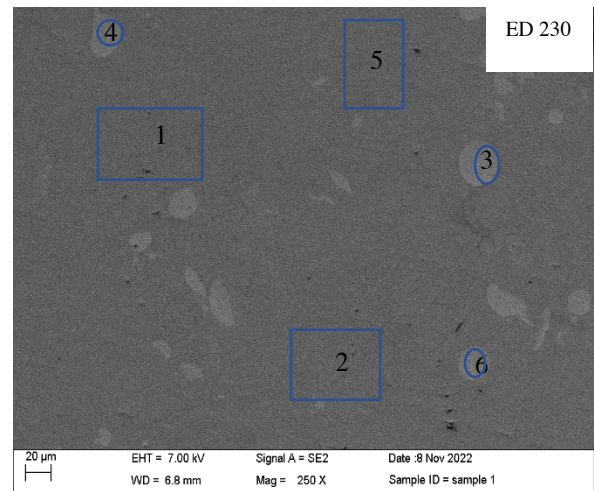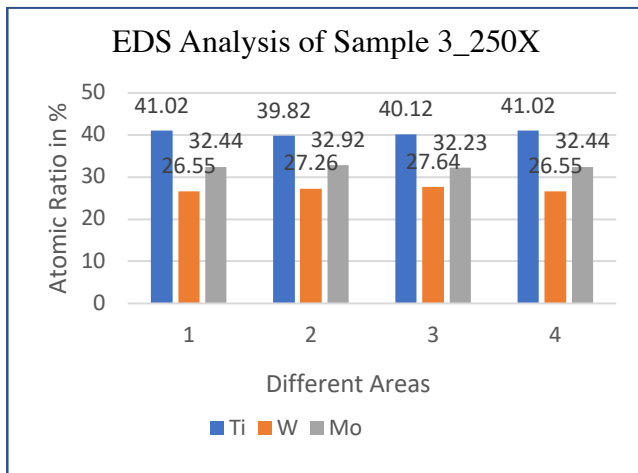
Figure 19: SEM images in higher magnification for (a) sample 3 and (b) sample 1, EDS analysis in different areas (c) sample 3 and (d) sample 1

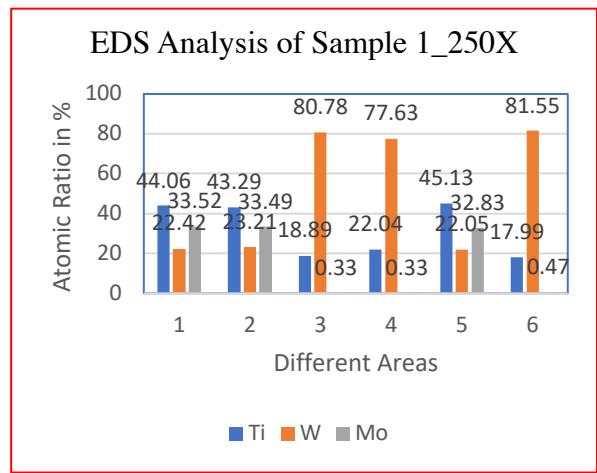Figure 20 indicated that the higher energy density gives less partially melted tungsten. Among the three elements, tungsten has the highest melting temperature (3420^0C) and Ti has the lowest melting temperature (1668^0C). According to the gaussian heat source, the energy is the highest in the center. This high energy is enough to melt the tungsten particle. However, the far point from the center has lower energy. This lower energy is not sufficient to melt the tungsten particles. As a result, some partially unmelted tungsten was remaining(K. Liu, Gu, Guo, & Sun, 2022). The side surface and the top surface of the samples in the figure 17 seems lots of unmelted particles. This is due to the low energy applied through the contour and in the last 3 layers of the full build.

In test 2 – 4, the atomic percentages of the elements were higher than expected. The titanium ratio was around 60-80%, molybdenum and tungsten were 10-28 % and 2-9% respectively. Additionally, the iron was present in the sample. Therefore, mixing the powder properly is very important and needs to be done properly. In order to mix the new powder properly the parameter of the mixing has been followed through the guidance. The volume of the powder inside the mixing chamber was less than 40% of the total volume. The mixing time was more than 12 hours.

To investigate the atomic ratios throughout the cross-section of each sample, a bunch of areas was considered from the bottom to the top surface. In figure 22, to check the composition throughout the cross-section, different areas were selected. The AB is the building direction. AC is estimated bottom layers. The blue bar is representing the 0.9 mm length. For samples 1, 2, 3 and 4 there are 11, 15, 13 and 12 areas taken respectively. AC axis is considered as 0 positions. The elemental distribution is represented in figure 23. In image 23 (a), initially at the bottom layers, the titanium ratio is 80%. As the substrate is titanium so more titanium particles are depleted from the substrate which increased the atomic percentage. Gradually with the distance of the areas from the AC axis. The titanium ratio is decreasing. And more molybdenum and tungsten particles are taking place in the built product. As a result, the composition of the elements is more stable from 0.7 onward. In sample 1, the titanium, tungsten and molybdenum are more stable at 41%, 26% and 33% respectively. Likewise, in sample 2 and sample 3 gave the same result.
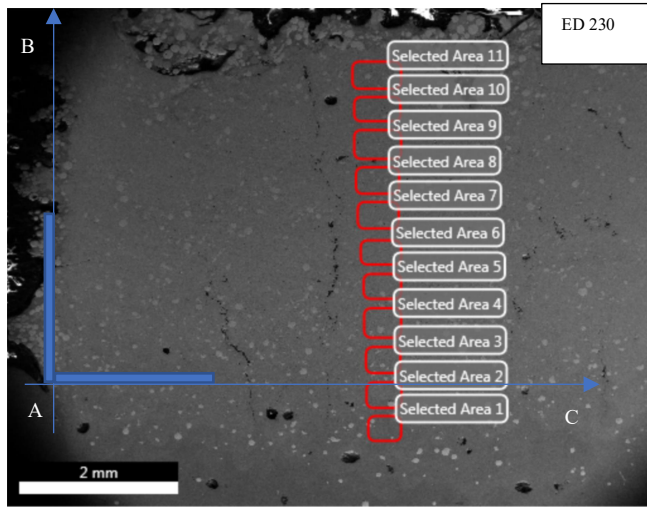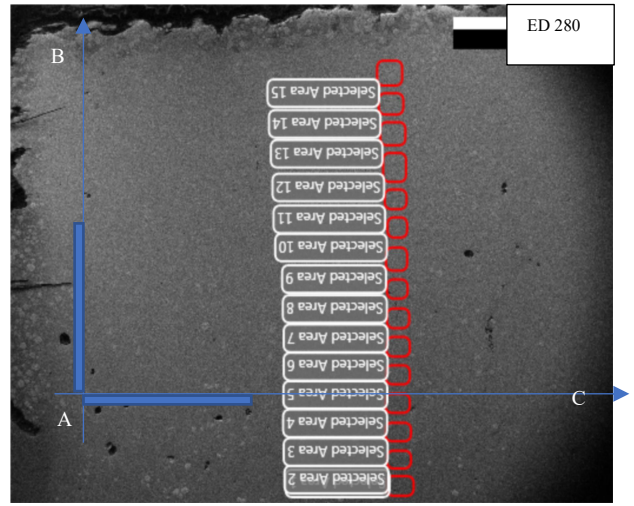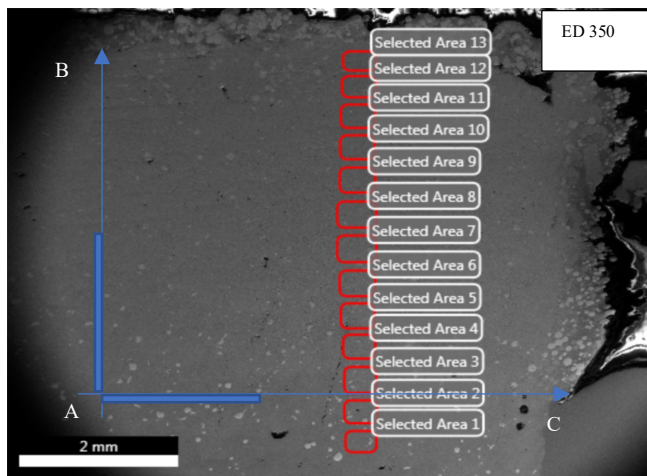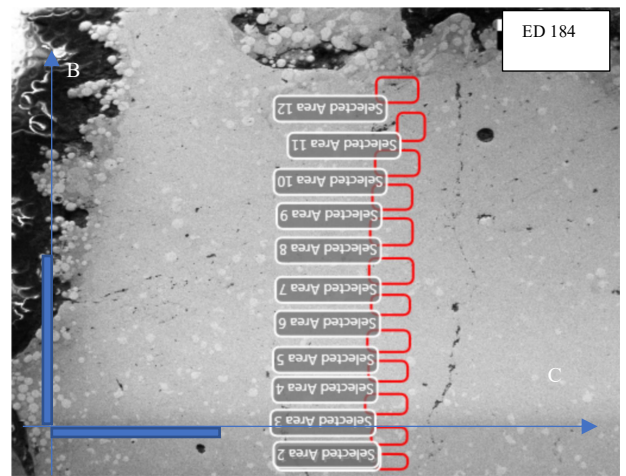
Figure 20: EDS analysis of different areas through the cross-section of the samples (a) sample 1, (b) sample 2, (c) sample 3 and (d) sample 4

(a)

(b)

(c)
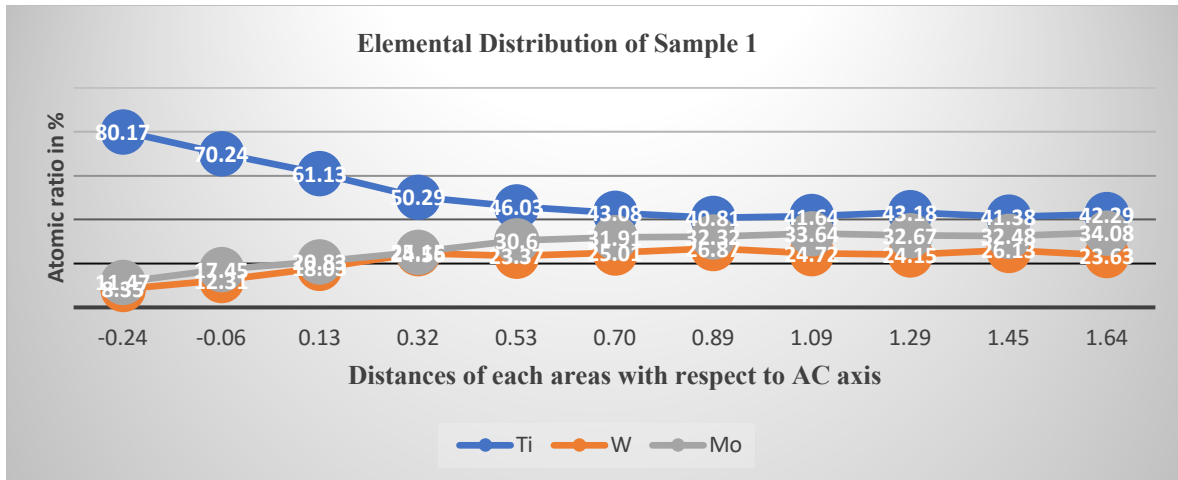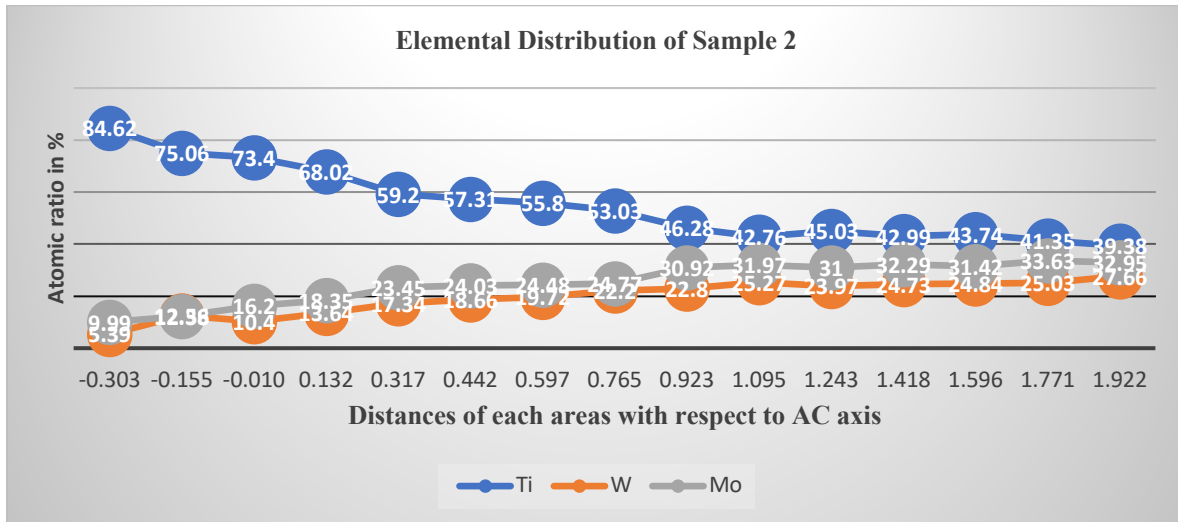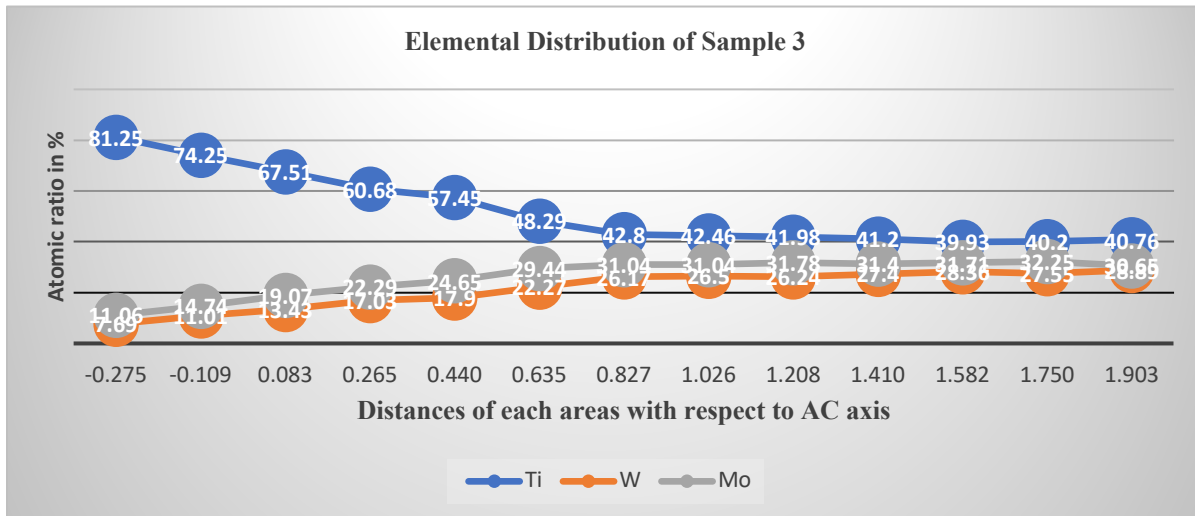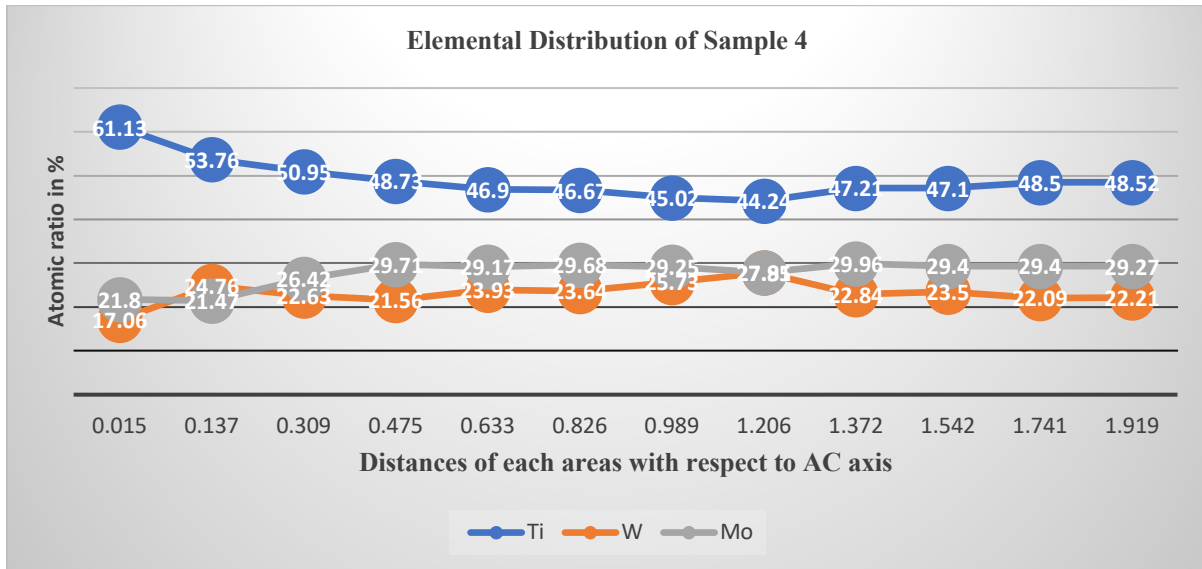
Figure 21: Atomic ratios of Ti, W and Mo into 4 samples through the cross-section. (a)sample 1, (b) sample 2, (c) sample 3 and (d) sample 4.

The unmelted tungsten also improved with lowering the scanning speed and increasing the laser power. In figure 24, at 250 mm/s speed the unmelted tungsten reduced to 1.14% and 1.72% at sample 3 and sample 2 respectively. Additionally, with increasing the laser power the unmelted tungsten also decreased. At 350W the laser power decreased more.
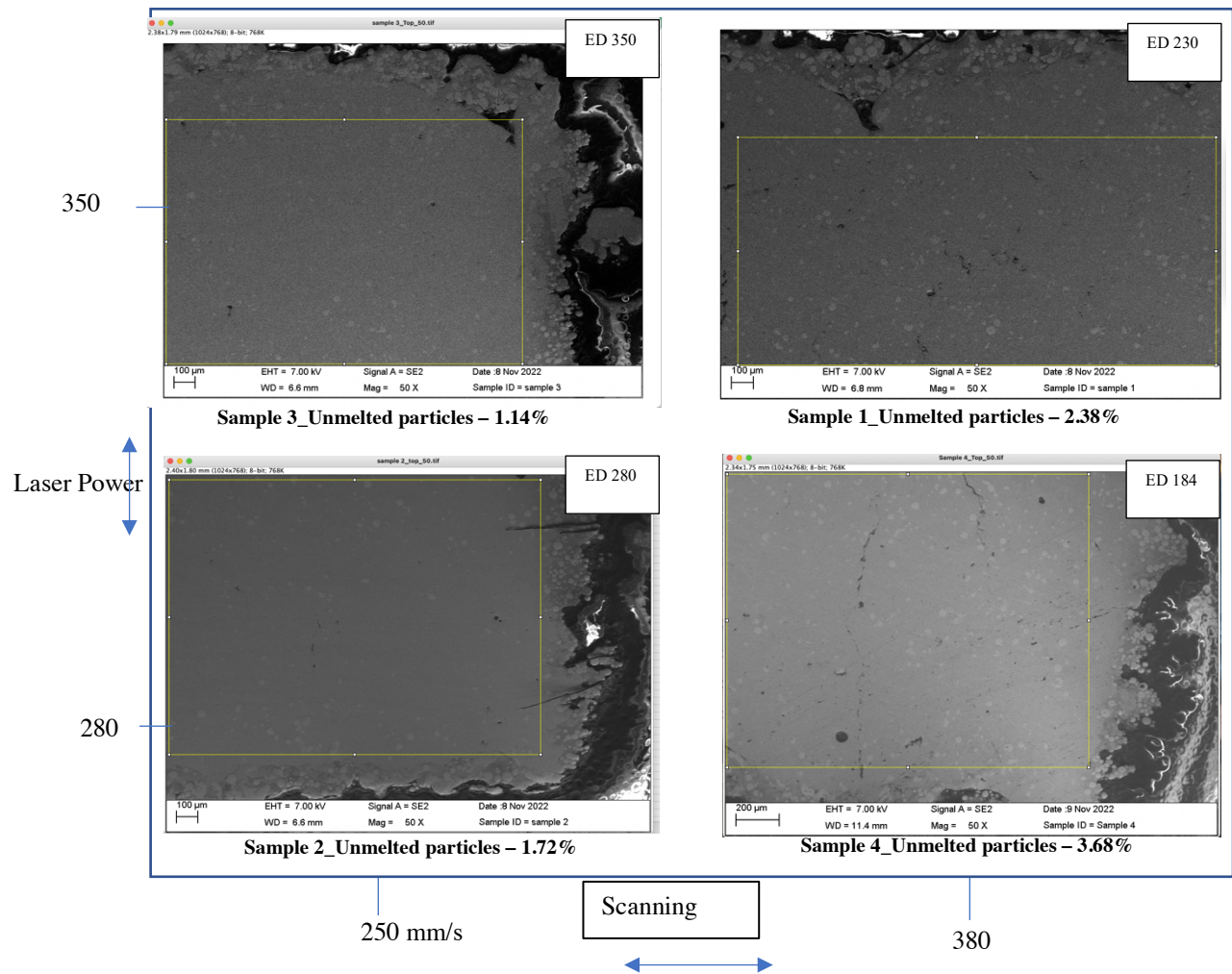
Figure 22: Impact of the energy density on the unmelted particles of TiWMo RMEA

4.6 Phase Prediction of TiWMo Sample on Titanium Substrate

Reference studies have been done on the phase stability and composition of several elements in high-entropy alloys. The random solid solution phase composition of medium and high-entropy alloys is often calculated using a number of specialized factors. Those are described below.

As per H-R rules, to get complete solubility, the atomic radius of each element in a binary solution must not differ more than 15% **(Massalski, Okamoto, Subramanian, Kacprzak, & Scott, 1986)**. Every three elements are compatible and might show good solubility in the alloy.

Table 9: Atomic radius of each element

	Tungsten	Molybdenum	Titanium
Atomic Radius (Angstrom)	1.39	1.39	1.47
7%	1.49425	1.49425	1.58025
-7%	1.28575	1.28575	1.35975

The atomic size difference can be calculated by the below equation(Y. Zhang, Yang, & Liaw, 2012):

$$Atomic\ Size\ Difference,\ \delta = 100 *$$

$$\sqrt{\sum_{i=1}^{n} Ci \left(1 - ri \frac{1}{\sum_{j=1}^{n} cj} rj\right)^2} \ldots\ldots\ldots\ldots\ldots\ldots\ldots\ldots\ldots\ldots\ldots\ldots(5)$$

Where, valence electron concentration (VEC) can be calculated(S. Guo, Ng, Lu, & Liu, 2011):

$$VEC = \sum_{i=1}^{n} c_i(VEC)_i \ldots\ldots\ldots\ldots\ldots\ldots\ldots\ldots\ldots\ldots\ldots(6)$$

Parameter $\Omega \geq 1.1$ (Y. Zhang et al., 2012):

Here $\mathbf{\Omega}$ defined as $\quad \Omega = T_m\Delta S_{mix} / \Delta H_{mix.} \ldots\ldots\ldots\ldots\ldots\ldots\ldots(7)$

With $T_m = \sum_{i=1}^{n} c_i (T)i$

T_m is the melting temperature of the i-th element, ΔS_{mix} and ΔH_{mix} the entropy and enthalpy of mixing predicted from Miedema theory.

The mixing enthalpy ΔH_{mix} can be calculated (S. Guo et al., 2011)

Here, ΔH_{mix} is given by, $\quad \sum_{i=1, j>i}^{n} 4 \Delta H^{mix} ABcicj$ (S. Guo et al., 2011)\ldots\ldots\ldots\ldots\ldots(8)

where ΔH_{mix} AB is the enthalpy of mixing for the binary AB equiatomic AB alloys.

Based on equation (5), (6), (7) and (8) the calculated atomic size different, valence electron concentration, Ω and mixing enthalpy of TiWMo alloy is 2.85%, 5.28, 5898 and -4.356 Kj/mole respectively. To get single phase solid solution, the atomic size difference needs to be less than 6.6%, $\Omega \geq 1.1$, mixing enthalpy needs to be $-20 \leq \Delta H_{mix} \geq 5$ kJ/mol. Therefore, TiWMo alloy meeting the single-phase solid solution requirements. Additionally, (VEC) ≥ 8 for fcc solid solutions and VEC < 6.87 for bcc phases. TiWMo alloy's VEC is indicating stable bcc solid solution phase.

4.7 Microhardness Testing of TiWMo

.The mirror polished sample was taken to the hardness testing machine. Diamond shape intender was placed on the surface of sample 1. The dwell time was 5 seconds. The force was 2.942N. This way three tests were done for each sample. The result of the microhardness of four different energy densities is displayed in figure 25. The picture depicts that the microhardness is proportionally related to the energy density. With the increase in energy density at 350 J/mm3, the microhardness is the highest. One of the reasons for the increased microhardness could be the more homogenous mixture and less partially melted tungsten in sample 3. The higher energy density took more time to melt the TiWMo powders and created less partially melted tungsten. With the lowest energy density 184 J/mm^3, the partially melted tungsten is more in sample 4. Which resulted in a lower microhardness value. Additionally, from figure 18, the pores are reduced with increasing energy density. Higher energy density provided sufficient heat to melt the powder in order to reduce the irregularly shaped pores (Pasebani, Ghayoor, Badwe, Irrinki, & Atre, 2018). In figure 27, the other research worked on RHEA and RMEA are referenced. The orange color is representing our work, which is promising.

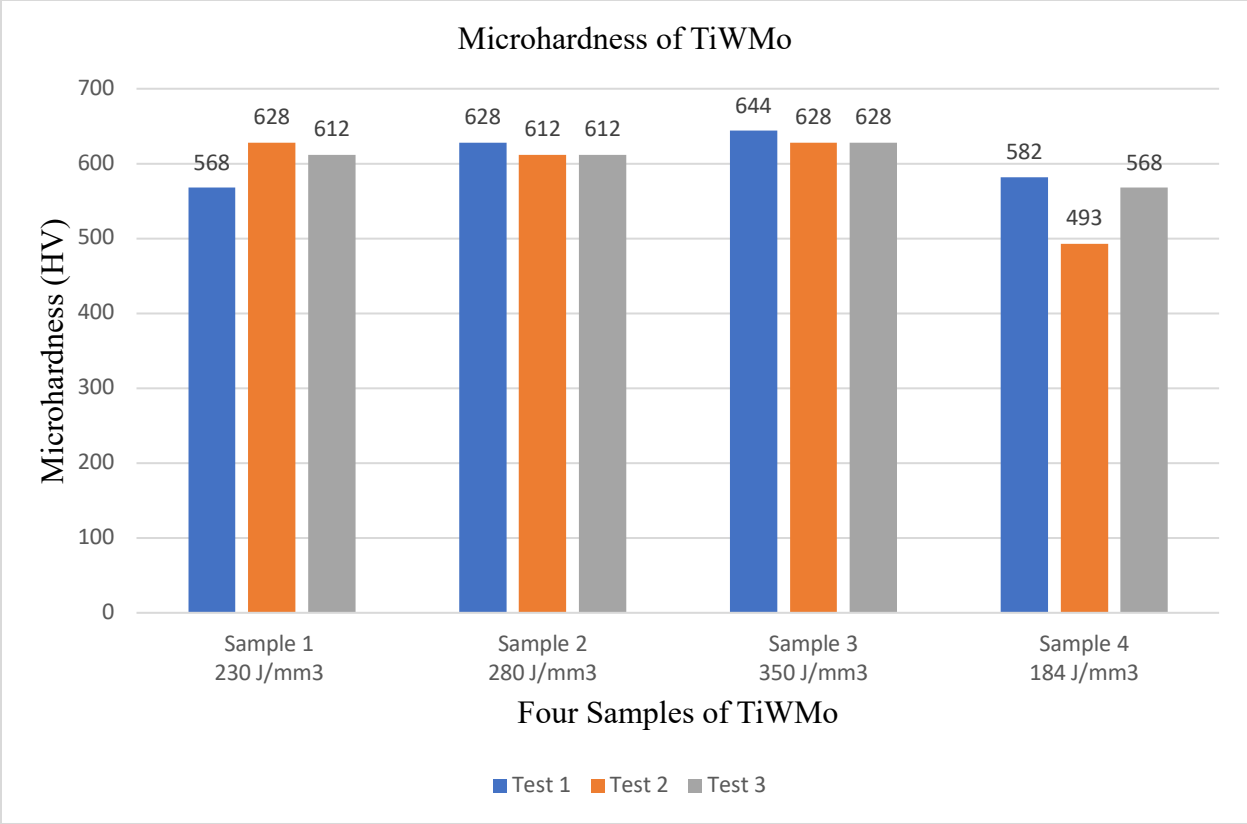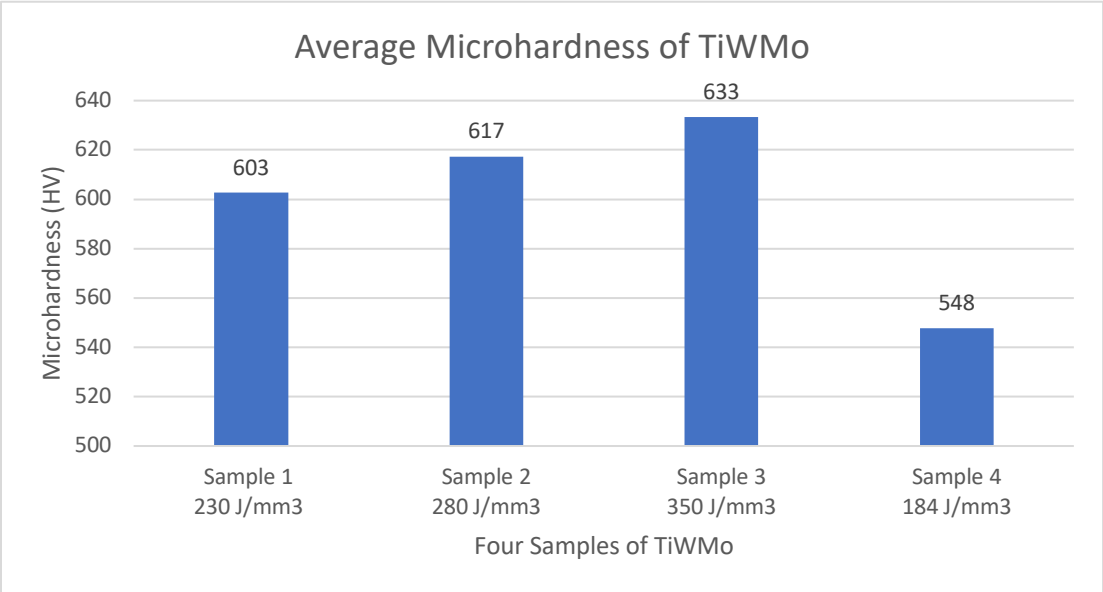Figure 25: Microhardness testing for TiWMo samples

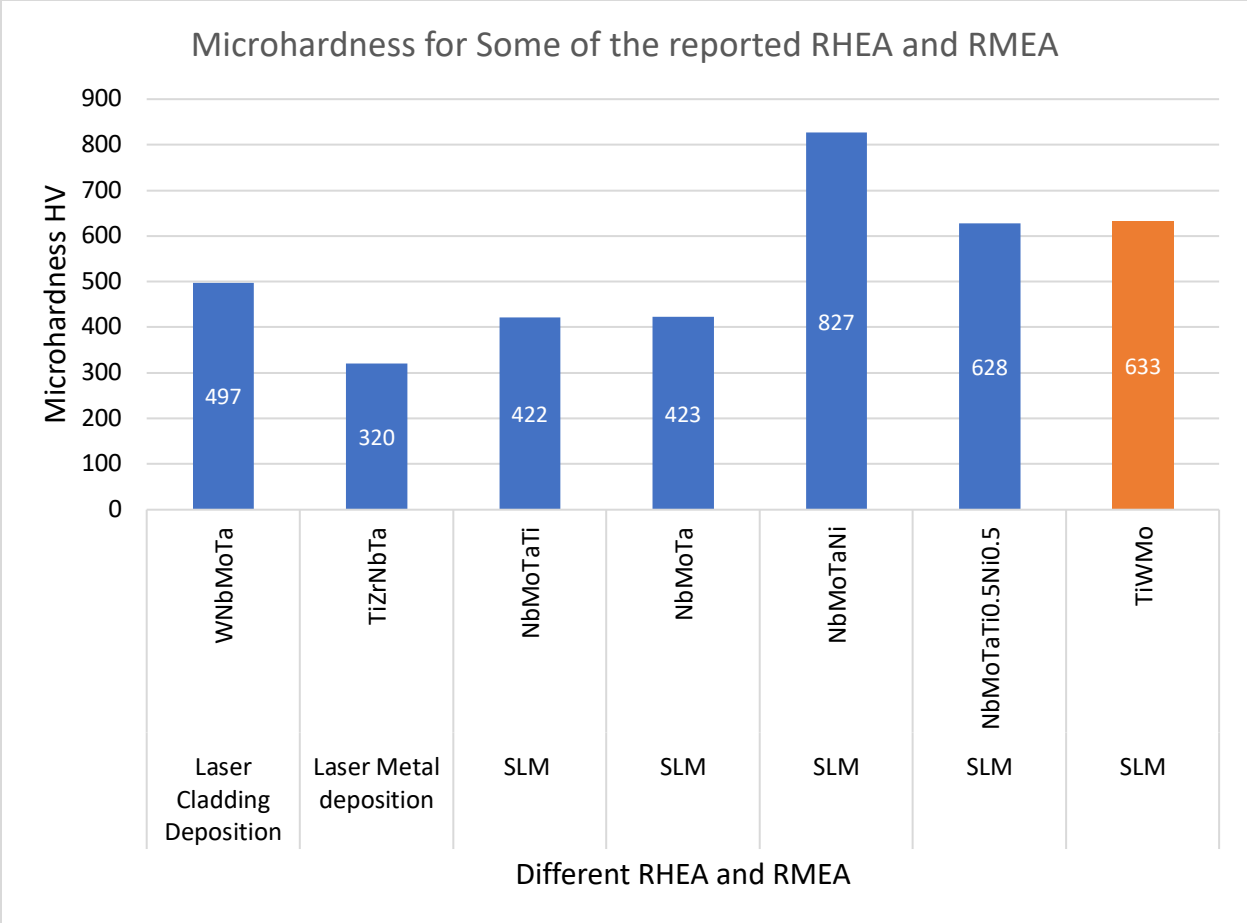Figure 26 : Average microhardness of TiWMo

Figure 27: Summary of microhardness for the commonly reported RHEA including this work (Dobbelstein, Gurevich, George, Ostendorf, & Laplanche, 2019; Huber, Bartels, & Schmidt, 2021; Li et al., 2019; Qiao et al., 2020; O. N. Senkov, Wilks, Scott, & Miracle, 2011; Yao et al., 2016; H. Zhang et al., 2021).

CHAPTER V

CONCLUSIONS

In this research project, we fabricated TiWMo refractory medium entropy alloy by selective laser melting process from the elemental powder. The powder was mixed with V shape mixer. EOS M290 machine printed the 5mm X 5mm X 2 mm sample. Steel, titanium and tungsten substrate were used to fabricate the samples. Different laser power and scanning speeds are considered to print this alloy. SEM and EDS analysis was done to check the microstructure and elemental distribution of TiWMo RMEA. The phase was predicted based on the theoretical calculation. A Microhardness test was done to check the mechanical properties. The main conclusion can be summarized below.

(1) Steel substrate made the printing fail as Fe reacted with the TiWMo alloy. Fe might react with Ti and could create TiFe and Fe_2Ti phases. Both phases are brittle in nature. Tungsten substrate also couldn't make the printing successful. As tungsten possess extremely high melting temperature as a result, many unmelted tungsten particles are created at the beginning of the printing which resulted in very less bonding between layers and failure to fabricate TiWMo RMEA. Only titanium substrate is supported to manufacture the TiWMo RMEA by selective laser melting process.

(2) The laser processing parameters greatly influenced the porosity of the sample. At the highest laser power 350W and lowest scanning speed 250 mm/s, the surface porosity measured was the least. So, decreasing the laser scanning speed gives more time to melt the elements and form the alloy. A lower energy density caused insufficient melting of tungsten particles, which created more pores.

(3) The SEM analysis could be divided into two findings. Most of the regions represented the homogeneous mixture and some bright areas represented partially melted tungsten. An increasing energy density reduced the partially melted tungsten. EDS analysis showed the

Ti atomic percentage was higher at the initial layers. After multiple layers of deposition (approximately 1 mm of height), composition was homogenized. The result indicates that stable deposition with constant composition were achieved.

(4) Single phase BCC is predicted based on the atomic size difference, valence electron concentration, mixing enthalpy and mixing entropy.

(5) The microhardness test results were influenced by higher energy density. The highest microhardness value was 644 HV at 350W laser power and 250 mm/s scanning speed. A higher energy density resulted in better densification and fewer pores and microcracks which resulted better hardness value.

REFERENCES

Airbus, S. (2014). Printing the future: Airbus expands its applications of the revolutionary additive layer manufacturing process. *Online. URL http://www. airbus. com/presscentre/pressreleases/press-release-detail/detail/printing-the-future-airbus-expands-itsapplications-of-the-revolutionary-additivelayer-manufacturi.*

Amirjan, M., & Sakiani, H. (2019). Effect of scanning strategy and speed on the microstructure and mechanical properties of selective laser melted IN718 nickel-based superalloy. *The International Journal of Advanced Manufacturing Technology, 103*(5), 1769-1780.

Attar, H., Bönisch, M., Calin, M., Zhang, L.-C., Scudino, S., & Eckert, J. (2014). Selective laser melting of in situ titanium–titanium boride composites: processing, microstructure and mechanical properties. *Acta Materialia, 76*, 13-22.

Attar, H., Ehtemam-Haghighi, S., Kent, D., Okulov, I., Wendrock, H., Bönisch, M., . . . Dargusch, M. (2017). Nanoindentation and wear properties of Ti and Ti-TiB composite materials produced by selective laser melting. *Materials Science and Engineering: A, 688*, 20-26.

Burns, N. (2014). Why AM now has the potential to revolutionise filtration solutions. *Filtration+ Separation, 51*(2), 42-43.

Cantor, B., Chang, I., Knight, P., & Vincent, A. (2004). Microstructural development in equiatomic multicomponent alloys. *Materials Science and Engineering: A, 375*, 213-218.

Carter, L. N., Martin, C., Withers, P. J., & Attallah, M. M. (2014). The influence of the laser scan strategy on grain structure and cracking behaviour in SLM powder-bed fabricated nickel superalloy. *Journal of Alloys and Compounds, 615*, 338-347.

Chen, H., Gu, D., Xiong, J., & Xia, M. (2017). Improving additive manufacturing processability of hard-to-process overhanging structure by selective laser melting. *Journal of Materials Processing Technology, 250*, 99-108.

Cheng, C.-Y., & Yeh, J.-W. (2016). High thermal stability of the amorphous structure of GexNbTaTiZr (x= 0.5, 1) high-entropy alloys. *Materials Letters, 181*, 223-226.

Chuang, M.-H., Tsai, M.-H., Wang, W.-R., Lin, S.-J., & Yeh, J.-W. (2011). Microstructure and wear behavior of AlxCo1. 5CrFeNi1. 5Tiy high-entropy alloys. *Acta Materialia, 59*(16), 6308-6317.

Ding, Q., Zhang, Y., Chen, X., Fu, X., Chen, D., Chen, S., . . . Gao, Y. (2019). Tuning element distribution, structure and properties by composition in high-entropy alloys. *Nature, 574*(7777), 223-227.

Dobbelstein, H., Gurevich, E. L., George, E. P., Ostendorf, A., & Laplanche, G. (2019). Laser metal deposition of compositionally graded TiZrNbTa refractory high-entropy alloys using elemental powder blends. *Additive Manufacturing, 25*, 252-262.

Dobbelstein, H., Thiele, M., Gurevich, E. L., George, E. P., & Ostendorf, A. (2016). Direct metal deposition of refractory high entropy alloy MoNbTaW. *Physics Procedia, 83*, 624-633.

Dong, Z., Liu, Y., Wen, W., Ge, J., & Liang, J. (2019). Effect of hatch spacing on melt pool and as-built quality during selective laser melting of stainless steel: Modeling and experimental approaches. *Materials, 12*(1), 50.

Enneti, R. K., Morgan, R., & Atre, S. V. (2018). Effect of process parameters on the Selective Laser Melting (SLM) of tungsten. *International Journal of Refractory Metals and Hard Materials, 71*, 315-319.

Essienubong, I. A., Ikechukwu, O., Ebunilo, P. O., & Ikpe, E. (2016). Material selection for high pressure (HP) turbine blade of conventional turbojet engines. *American journal of mechanical and industrial engineering, 1*(1), 1.

Fultz, B. (2010). Vibrational thermodynamics of materials. *Progress in Materials Science, 55*(4), 247-352.

Gludovatz, B., Hohenwarter, A., Thurston, K. V., Bei, H., Wu, Z., George, E. P., & Ritchie, R. O. (2016). Exceptional damage-tolerance of a medium-entropy alloy CrCoNi at cryogenic temperatures. *Nature communications, 7*(1), 1-8.

Gong, H., Rafi, K., Gu, H., Ram, G. J., Starr, T., & Stucker, B. (2015). Influence of defects on mechanical properties of Ti–6Al–4 V components produced by selective laser melting and electron beam melting. *Materials & Design, 86*, 545-554.

Gorsse, S., Miracle, D. B., & Senkov, O. N. (2017). Mapping the world of complex concentrated alloys. *Acta Materialia, 135*, 177-187.

Gu, D., Hagedorn, Y.-C., Meiners, W., Meng, G., Batista, R. J. S., Wissenbach, K., & Poprawe, R. (2012). Densification behavior, microstructure evolution, and wear performance of selective laser melting processed commercially pure titanium. *Acta Materialia, 60*(9), 3849-3860.

Gu, D. D., Meiners, W., Wissenbach, K., & Poprawe, R. (2012). Laser additive manufacturing of metallic components: materials, processes and mechanisms. *International Materials Reviews, 57*(3), 133-164.

Gu, S., & Olivier, H. (2020). Capabilities and limitations of existing hypersonic facilities. *Progress in Aerospace Sciences, 113*, 100607.

Guo, L., Gu, J., Gan, B., Ni, S., Bi, Z., Wang, Z., & Song, M. (2021). Effects of elemental segregation and scanning strategy on the mechanical properties and hot cracking of a selective laser melted FeCoCrNiMn-(N, Si) high entropy alloy. *Journal of Alloys and Compounds, 865*, 158892.

Guo, M., Gu, D., Xi, L., Du, L., Zhang, H., & Zhang, J. (2019). Formation of scanning tracks during Selective Laser Melting (SLM) of pure tungsten powder: Morphology, geometric features and forming mechanisms. *International Journal of Refractory Metals and Hard Materials, 79*, 37-46.

Guo, M., Ye, Y., Jiang, X., & Wang, L. (2019). Microstructure, mechanical properties and residual stress of selective laser melted AlSi10Mg. *Journal of Materials Engineering and Performance, 28*(11), 6753-6760.

Guo, S., Ng, C., Lu, J., & Liu, C. (2011). Effect of valence electron concentration on stability of fcc or bcc phase in high entropy alloys. *Journal of Applied Physics, 109*(10), 103505.

Guo, W., Liu, B., Liu, Y., Li, T., Fu, A., Fang, Q., & Nie, Y. (2019). Microstructures and mechanical properties of ductile NbTaTiV refractory high entropy alloy prepared by powder metallurgy. *Journal of Alloys and Compounds, 776*, 428-436.

Guo, Z., Wang, L., Wang, C., Ding, X., & Liu, J. (2020). Heat Transfer, Molten Pool Flow Micro-Simulation, and Experimental Research on Molybdenum Alloys Fabricated via Selective Laser Melting. *Materials, 14*(1), 75.

Han, Z., Luan, H., Liu, X., Chen, N., Li, X., Shao, Y., & Yao, K. (2018). Microstructures and mechanical properties of TixNbMoTaW refractory high-entropy alloys. *Materials Science and Engineering: A, 712*, 380-385.

He, K., & Zhao, X. (2018). 3D thermal finite element analysis of the SLM 316L parts with microstructural correlations. *Complexity, 2018*.

He, Q., Yoshida, S., Yasuda, H., & Tsuji, N. (2020). Effect of elemental combination on microstructure and mechanical properties of quaternary refractory medium entropy alloys. *Materials Transactions*, MT-MK2019003.

Hemphill, M. A., Yuan, T., Wang, G., Yeh, J., Tsai, C., Chuang, A., & Liaw, P. (2012). Fatigue behavior of Al0. 5CoCrCuFeNi high entropy alloys. *Acta Materialia, 60*(16), 5723-5734.

Huang, J., & Yao, W.-X. (2020). Active flow control by a novel combinational active thermal protection for hypersonic vehicles. *Acta Astronautica, 170*, 320-330.

Huang, P. K., Yeh, J. W., Shun, T. T., & Chen, S. K. (2004). Multi-principal-element alloys with improved oxidation and wear resistance for thermal spray coating. *Advanced Engineering Materials, 6*(1-2), 74-78.

Huber, F., Bartels, D., & Schmidt, M. (2021). In-situ alloy formation of a WMoTaNbV refractory metal high entropy alloy by laser powder bed fusion (PBF-LB/M). *Materials, 14*(11), 3095.

Iveković, A., Montero-Sistiaga, M. L., Vanmeensel, K., Kruth, J.-P., & Vleugels, J. (2019). Effect of processing parameters on microstructure and properties of tungsten heavy alloys fabricated by SLM. *International Journal of Refractory Metals and Hard Materials, 82*, 23-30.

Jia, H., Sun, H., Wang, H., Wu, Y., & Wang, H. (2021). Scanning strategy in selective laser melting (SLM): a review. *The International Journal of Advanced Manufacturing Technology, 113*(9), 2413-2435.

Kaciulis, S., Mezzi, A., Amati, M., Montanari, R., Angella, G., & Maldini, M. (2012). Relation between the microstructure and microchemistry in Ni-based superalloy. *Surface and interface analysis, 44*(8), 982-985.

Kang, B., Lee, J., Ryu, H. J., & Hong, S. H. (2018). Ultra-high strength WNbMoTaV high-entropy alloys with fine grain structure fabricated by powder metallurgical process. *Materials Science and Engineering: A, 712*, 616-624.

Kasperovich, G., & Hausmann, J. (2015). Improvement of fatigue resistance and ductility of TiAl6V4 processed by selective laser melting. *Journal of Materials Processing Technology, 220*, 202-214.

Kim, Y.-K., Baek, M.-S., Yang, S., & Lee, K.-A. (2021). In-situ formed oxide enables extraordinary high-cycle fatigue resistance in additively manufactured CoCrFeMnNi high-entropy alloy. *Additive Manufacturing, 38*, 101832.

Kruth, J.-P., Froyen, L., Van Vaerenbergh, J., Mercelis, P., Rombouts, M., & Lauwers, B. (2004). Selective laser melting of iron-based powder. *Journal of Materials Processing Technology, 149*(1-3), 616-622.

Li, Q., Zhang, H., Li, D., Chen, Z., Huang, S., Lu, Z., & Yan, H. (2019). W x NbMoTa refractory high-entropy alloys fabricated by laser cladding deposition. *Materials, 12*(3), 533.

Litwa, P., Hernandez-Nava, E., Guan, D., Goodall, R., & Wika, K. K. (2021). The additive manufacture processing and machinability of CrMnFeCoNi high entropy alloy. *Materials & Design, 198*, 109380.

Liu, B., Wang, J., Chen, J., Fang, Q., & Liu, Y. (2017). Ultra-high strength TiC/refractory high-entropy-alloy composite prepared by powder metallurgy. *Jom, 69*(4), 651-656.

Liu, C., Zhu, K., Ding, W., Liu, Y., Chen, G., & Qu, X. (2022). Additive manufacturing of WMoTaTi refractory high-entropy alloy by employing fluidised powders. *Powder Metallurgy*, 1-13.

Liu, K., Gu, D., Guo, M., & Sun, J. (2022). Effects of processing parameters on densification behavior, microstructure evolution and mechanical properties of W–Ti alloy fabricated by laser powder bed fusion. *Materials Science and Engineering: A, 829*, 142177.

Louzguine-Luzgin, D. V. (2018). High-strength Ti-based alloys containing Fe as one of the main alloying elements. *Materials Transactions*, M2018114.

Lu, Y., Dong, Y., Guo, S., Jiang, L., Kang, H., Wang, T., . . . Cao, Z. (2014). A promising new class of high-temperature alloys: eutectic high-entropy alloys. *Scientific reports, 4*(1), 1-5.

Lu, Y., Wu, S., Gan, Y., Huang, T., Yang, C., Junjie, L., & Lin, J. (2015). Study on the microstructure, mechanical property and residual stress of SLM Inconel-718 alloy manufactured by differing island scanning strategy. *Optics & Laser Technology, 75*, 197-206.

Luo, S., Gao, P., Yu, H., Yang, J., Wang, Z., & Zeng, X. (2019). Selective laser melting of an equiatomic AlCrCuFeNi high-entropy alloy: Processability, non-equilibrium microstructure and mechanical behavior. *Journal of Alloys and Compounds, 771*, 387-397.

Massalski, T. B., Okamoto, H., Subramanian, P., Kacprzak, L., & Scott, W. W. (1986). *Binary alloy phase diagrams* (Vol. 1): American society for metals Metals Park, OH.

Miracle, D. B., Miller, J. D., Senkov, O. N., Woodward, C., Uchic, M. D., & Tiley, J. (2014). Exploration and development of high entropy alloys for structural applications. *Entropy, 16*(1), 494-525.

Miracle, D. B., & Senkov, O. N. (2017). A critical review of high entropy alloys and related concepts. *Acta Materialia, 122*, 448-511.

Mo, D.-f., Song, T.-f., Fang, Y.-j., Jiang, X.-s., Luo, C. Q., Simpson, M. D., & Luo, Z.-p. (2018). A review on diffusion bonding between titanium alloys and stainless steels. *Advances in Materials Science and Engineering, 2018*.

Moghaddam, A. O., Shaburova, N. A., Samodurova, M. N., Abdollahzadeh, A., & Trofimov, E. A. (2021). Additive manufacturing of high entropy alloys: A practical review. *Journal of Materials Science & Technology, 77*, 131-162.

Nguyen, V., Qian, M., Shi, Z., Song, T., Huang, L., & Zou, J. (2018). A novel quaternary equiatomic Ti-Zr-Nb-Ta medium entropy alloy (MEA). *Intermetallics, 101*, 39-43.

Nickels, L. (2016). Meeting the mainstream. *Metal Powder Report, 71*(3), 169-171.

Pasebani, S., Ghayoor, M., Badwe, S., Irrinki, H., & Atre, S. V. (2018). Effects of atomizing media and post processing on mechanical properties of 17-4 PH stainless steel manufactured via selective laser melting. *Additive Manufacturing, 22*, 127-137.

Perepezko, J. H. (2009). The hotter the engine, the better. *Science, 326*(5956), 1068-1069.

Pickering, E., & Jones, N. (2016). High-entropy alloys: a critical assessment of their founding principles and future prospects. *International Materials Reviews, 61*(3), 183-202.

Promoppatum, P., & Yao, S.-C. (2020). Influence of scanning length and energy input on residual stress reduction in metal additive manufacturing: Numerical and experimental studies. *Journal of Manufacturing Processes, 49*, 247-259.

Pupo, Y., Delgado, J., Serenó, L., & Ciurana, J. (2013). Scanning space analysis in selective laser melting for CoCrMo powder. *Procedia Engineering, 63*, 370-378.

Qiao, Y., Tang, Y., Li, S., Ye, Y., Liu, X., & Bai, S. (2020). Preparation of TiZrNbTa refractory high-entropy alloy powder by mechanical alloying with liquid process control agents. *Intermetallics, 126*, 106900.

Raabe, D., Ponge, D., Dmitrieva, O., & Sander, B. (2009). Nanoprecipitate-hardened 1.5 GPa steels with unexpected high ductility. *Scripta Materialia, 60*(12), 1141-1144.

Ramos, D., Belblidia, F., & Sienz, J. (2019). New scanning strategy to reduce warpage in additive manufacturing. *Additive Manufacturing, 28*, 554-564.

Rao, H., Giet, S., Yang, K., Wu, X., & Davies, C. H. (2016). The influence of processing parameters on aluminium alloy A357 manufactured by Selective Laser Melting. *Materials & Design, 109*, 334-346.

Ren, X., Liu, H., Lu, F., Huang, L., & Yi, X. (2021). Effects of processing parameters on the densification, microstructure and mechanical properties of pure tungsten fabricated by optimized selective laser melting: From single and multiple scan tracks to bulk parts. *International Journal of Refractory Metals and Hard Materials, 96*, 105490.

Sateesh, N., Kumar, G. M., Prasad, K., Srinivasa, C., & Vinod, A. (2014). Microstructure and mechanical characterization of laser sintered Inconel-625 superalloy. *Procedia Materials Science, 5*, 772-779.

Senkov, O., Senkova, S., Dimiduk, D., Woodward, C., & Miracle, D. (2012). Oxidation behavior of a refractory NbCrMo 0.5 Ta 0.5 TiZr alloy. *Journal of Materials Science, 47*(18), 6522-6534.

Senkov, O., Wilks, G., Miracle, D., Chuang, C., & Liaw, P. (2010). Refractory high-entropy alloys. *Intermetallics, 18*(9), 1758-1765.

Senkov, O. N., Miracle, D. B., Chaput, K. J., & Couzinie, J.-P. (2018). Development and exploration of refractory high entropy alloys—A review. *Journal of materials research, 33*(19), 3092-3128.

Senkov, O. N., Wilks, G., Scott, J., & Miracle, D. B. (2011). Mechanical properties of Nb25Mo25Ta25W25 and V20Nb20Mo20Ta20W20 refractory high entropy alloys. *Intermetallics, 19*(5), 698-706.

Su, I.-A., Tseng, K.-K., Yeh, J.-W., El-Sayed, B., Liu, C.-H., & Wang, S.-H. (2022). Strengthening mechanisms and microstructural evolution of ductile refractory medium-entropy alloy Hf20Nb10Ti35Zr35. *Scripta Materialia, 206*, 114225.

Suryanarayana, C. (2001). Mechanical alloying and milling. *Progress in Materials Science, 46*(1-2), 1-184.

Swalin, R. A., & Arents, J. (1962). Thermodynamics of solids. *Journal of The Electrochemical Society, 109*(12), 308C.

Tian, S.-G., Liang, F.-S., Li, A.-N., Li, J.-J., & Qian, B.-J. (2011). Microstructure evolution and deformation features of single crystal nickel-based superalloy containing 4.2% Re during creep. *Transactions of Nonferrous Metals Society of China, 21*(7), 1532-1537.

Trosch, T., Strößner, J., Völkl, R., & Glatzel, U. (2016). Microstructure and mechanical properties of selective laser melted Inconel 718 compared to forging and casting. *Materials Letters, 164*, 428-431.

Tsai, M.-H., & Yeh, J.-W. (2014). High-entropy alloys: a critical review. *Materials Research Letters, 2*(3), 107-123.

Vayssette, B., Saintier, N., Brugger, C., Elmay, M., & Pessard, E. (2018). Surface roughness of Ti-6Al-4V parts obtained by SLM and EBM: Effect on the High Cycle Fatigue life. *Procedia Engineering, 213*, 89-97.

Wang, L., Jiang, X., Zhu, Y., Zhu, X., Sun, J., & Yan, B. (2018). An approach to predict the residual stress and distortion during the selective laser melting of AlSi10Mg parts. *The International Journal of Advanced Manufacturing Technology, 97*(9), 3535-3546.

Wang, S.-P., Ma, E., & Xu, J. (2019). New ternary equi-atomic refractory medium-entropy alloys with tensile ductility: Hafnium versus titanium into NbTa-based solution. *Intermetallics, 107*, 15-23.

Wang, W., Jin, T., Liu, J., Sun, X., Guan, H., & Hu, Z. (2008). Role of Re and Co on microstructures and γ' coarsening in single crystal superalloys. *Materials Science and Engineering: A, 479*(1-2), 148-156.

Wang, X. F., Wang, X. G., Yang, Q. Q., Dong, H. L., Zhang, C., Zhang, G. J., & Jiang, D. Y. (2021). High-strength medium-entropy (Ti, Zr, Hf) C ceramics up to 1800° C. *Journal of the American Ceramic Society, 104*(6), 2436-2441.

Waseem, O. A., Lee, J., Lee, H. M., & Ryu, H. J. (2018). The effect of Ti on the sintering and mechanical properties of refractory high-entropy alloy TixWTaVCr fabricated via spark plasma sintering for fusion plasma-facing materials. *Materials Chemistry and Physics, 210*, 87-94.

Wu, Y., Cai, Y., Wang, T., Si, J., Zhu, J., Wang, Y., & Hui, X. (2014). A refractory Hf25Nb25Ti25Zr25 high-entropy alloy with excellent structural stability and tensile properties. *Materials Letters, 130*, 277-280.

Wu, Z., Bei, H., Pharr, G. M., & George, E. P. (2014). Temperature dependence of the mechanical properties of equiatomic solid solution alloys with face-centered cubic crystal structures. *Acta Materialia, 81*, 428-441.

Xie, D., Dong, B., & Jing, X. (2020). Effect of thermal protection system size on aerothermoelastic stability of the hypersonic panel. *Aerospace Science and Technology, 106*, 106170.

Xiong, W., Hao, L., Li, Y., Tang, D., Cui, Q., Feng, Z., & Yan, C. (2019). Effect of selective laser melting parameters on morphology, microstructure, densification and mechanical properties of supersaturated silver alloy. *Materials & Design, 170*, 107697.

Yao, H., Qiao, J., Gao, M., Hawk, J., Ma, S., Zhou, H., & Zhang, Y. (2016). NbTaV-(Ti, W) refractory high-entropy alloys: experiments and modeling. *Materials Science and Engineering: A, 674*, 203-211.

Yeh, A., & Tin, S. (2005). Effects of Ru and Re additions on the high temperature flow stresses of Ni-base single crystal superalloys. *Scripta Materialia, 52*(6), 519-524.

Yeh, J.-W. (2013). Alloy design strategies and future trends in high-entropy alloys. *Jom, 65*(12), 1759-1771.

Yeh, J. W., Chen, S. K., Lin, S. J., Gan, J. Y., Chin, T. S., Shun, T. T., . . . Chang, S. Y. (2004). Nanostructured high-entropy alloys with multiple principal elements: novel alloy design concepts and outcomes. *Advanced Engineering Materials, 6*(5), 299-303.

Zaeh, M. F., & Branner, G. (2010). Investigations on residual stresses and deformations in selective laser melting. *Production Engineering, 4*(1), 35-45.

Zegzulka, J., Gelnar, D., Jezerska, L., Prokes, R., & Rozbroj, J. (2020). Characterization and flowability methods for metal powders. *Scientific reports, 10*(1), 1-19.

Zhang, B., Li, Y., & Bai, Q. (2017). Defect formation mechanisms in selective laser melting: a review. *Chinese Journal of Mechanical Engineering, 30*(3), 515-527.

Zhang, H., Xu, W., Xu, Y., Lu, Z., & Li, D. (2018). The thermal-mechanical behavior of WTaMoNb high-entropy alloy via selective laser melting (SLM): experiment and

simulation. *The International Journal of Advanced Manufacturing Technology, 96*(1), 461-474.

Zhang, H., Zhao, Y., Cai, J., Ji, S., Geng, J., Sun, X., & Li, D. (2021). High-strength NbMoTaX refractory high-entropy alloy with low stacking fault energy eutectic phase via laser additive manufacturing. *Materials & Design, 201*, 109462.

Zhang, H., Zhao, Y., Huang, S., Zhu, S., Wang, F., & Li, D. (2019). Manufacturing and analysis of high-performance refractory high-entropy alloy via selective laser melting (SLM). *Materials, 12*(5), 720.

Zhang, Y., Yang, X., & Liaw, P. (2012). Alloy design and properties optimization of high-entropy alloys. *Jom, 64*(7), 830-838.

Zhang, Z., Sheng, H., Wang, Z., Gludovatz, B., Zhang, Z., George, E. P., . . . Ritchie, R. O. (2017). Dislocation mechanisms and 3D twin architectures generate exceptional strength-ductility-toughness combination in CrCoNi medium-entropy alloy. *Nature communications, 8*(1), 1-8.

Zhou, L., Yuan, T., Li, R., Tang, J., Wang, G., & Guo, K. (2017). Selective laser melting of pure tantalum: densification, microstructure and mechanical behaviors. *Materials Science and Engineering: A, 707*, 443-451.

Zou, S., Xiao, H., Ye, F., Li, Z., Tang, W., Zhu, F., . . . Zhu, C. (2020). Numerical analysis of the effect of the scan strategy on the residual stress in the multi-laser selective laser melting. *Results in Physics, 16*, 103005.

BIOGRAPHICAL SKETCH

Abdullah Al Masum Jabir completed his bachelor's degree in Industrial and Production Engineering from the Bangladesh University of Engineering and Technology. Since then Jabir worked at Decathlon as a supply production leader for 3.5 years. After gathering excellent industrial and leadership experience, Jabir joined at the University of Texas Rio Grande Valley for pursuing master's in manufacturing engineering program. Additionally, he was awarded presidential graduate research assistant, his research focus was metal additive manufacturing. He used a selective laser melting process to manufacture ultrahard materials. Dr James Li was his supervisor. After completing the MSE in Manufacturing Engineering, Jabir wants to go back to the industry to have some real-world manufacturing experience. He can be reached at masum.jabir@gmail.com.